

Ketogenic HMG-CoA lyase and its product β -hydroxybutyrate promote pancreatic cancer progression

Victoire Gouirand^{1,2,3,4} , Tristan Gicquel^{1,2,3,4} , Evan C Lien⁵ , Emilie Jaune-Pons^{1,2,3,4} , Quentin Da Costa^{1,2,3,4} , Pascal Finetti^{1,2,3,4}, Elodie Metay^{1,2,3,4}, Camille Duluc^{1,2,3,4}, Jared R Mayers⁵ , Stephane Audebert^{1,2,3,4} , Luc Camoin^{1,2,3,4} , Laurence Borge^{1,2,3,4}, Marion Rubis^{1,2,3,4}, Julie Leca^{1,2,3,4} , Jeremy Nigri^{1,2,3,4} , Francois Bertucci^{1,2,3,4} , Nelson Dusetti^{1,2,3,4} , Juan Lucio Iovanna^{1,2,3,4} , Richard Tomasini^{1,2,3,4} , Ghislain Bidaut^{1,2,3,4} , Fabienne Guillaumond^{1,2,3,4} , Matthew G Vander Heiden^{5,6}  & Sophie Vasseur^{1,2,3,4,*} 

Abstract

Pancreatic ductal adenocarcinoma (PDA) tumor cells are deprived of oxygen and nutrients and therefore must adapt their metabolism to ensure proliferation. In some physiological states, cells rely on ketone bodies to satisfy their metabolic needs, especially during nutrient stress. Here, we show that PDA cells can activate ketone body metabolism and that β -hydroxybutyrate (β OHB) is an alternative cell-intrinsic or systemic fuel that can promote PDA growth and progression. PDA cells activate enzymes required for ketogenesis, utilizing various nutrients as carbon sources for ketone body formation. By assessing metabolic gene expression from spontaneously arising PDA tumors in mice, we find HMG-CoA lyase (HMGCL), involved in ketogenesis, to be among the most deregulated metabolic enzymes in PDA compared to normal pancreas. *In vitro* depletion of HMGCL impedes migration, tumor cell invasiveness, and anchorage-independent tumor sphere compaction. Moreover, disrupting HMGCL drastically decreases PDA tumor growth *in vivo*, while β OHB stimulates metastatic dissemination to the liver. These findings suggest that β OHB increases PDA aggressiveness and identify HMGCL and ketogenesis as metabolic targets for limiting PDA progression.

Keywords HMGCL; ketone bodies; metastasis; pancreatic cancer; β -hydroxybutyrate

Subject Categories Cancer; Immunology; Metabolism

DOI 10.15252/embj.2021110466 | Received 29 December 2021 | Revised 18 February 2022 | Accepted 24 February 2022 | Published online 21 March 2022

The EMBO Journal (2022) 41: e110466

Introduction

Among cancers, pancreatic ductal adenocarcinoma (PDA) is particularly deadly as almost 90% of PDA patients die from their disease in 5 years. PDA is predicted to become the third most common cause of cancer-related death in the European Union (Ferlay *et al*, 2016), a ranking already reached in the USA (Siegel *et al*, 2019). Among PDA patients, 80–85% are not eligible for a potentially curative surgical resection because of an unresectable tumor or presence of metastases, and chemotherapy remains the only therapeutic option with limited impact on overall survival (Mizrahi *et al*, 2020; O’Kane *et al*, 2021). This therapeutic void in part reflects an incomplete understanding of disease pathogenesis that limits opportunities to uncover new therapies. PDA tumors contain a dense extracellular matrix derived from non-cancerous stromal cells that limits vacularization and leads to poor oxygen and nutrient delivery to tumor cells (Guillaumond *et al*, 2013). Several studies have described the metabolic plasticity of pancreatic tumor cells and how these cells might adapt to the complex PDA microenvironment. For example, PDA cells can scavenge macromolecules from the microenvironment, including catabolism of the extracellular matrix to obtain amino acids and support tumor growth (Commissio *et al*, 2013; Kamphorst *et al*, 2015; Davidson *et al*, 2017; Olivares *et al*, 2017). PDA cells are also reliant on glucose, lactate, alanine, glutamine, and/or cysteine to sustain bioenergetics, limit ROS-induced damage, and fuel anabolism (Ying *et al*, 2012; Guillaumond *et al*, 2013; Chakrabarti *et al*, 2015; Daher *et al*, 2019; Badgley *et al*, 2020; Parker *et al*, 2020). This metabolic flexibility provides PDA tumor cells with the ability to adapt to glucose- and glutamine-deprived conditions and use

¹ Centre de Recherche en Cancérologie de Marseille (CRCM), Unité 1068, Institut National de la Santé et de la Recherche Médicale, Marseille, France

² Institut Paoli-Calmettes (IPC), Marseille, France

³ Unité Mixte de Recherche (UMR 7258), Centre National de la Recherche Scientifique (CNRS), Marseille, France

⁴ Université Aix-Marseille, Marseille, France

⁵ Department of Biology, Koch Institute for Integrative Cancer Research, Massachusetts Institute of Technology, Cambridge, MA, USA

⁶ Dana-Farber Cancer Institute, Boston, MA, USA

*Corresponding author (lead contact). Tel: +33 491 828 806; Fax: +33 491 826 083; E-mail: sophie.vasseur@inserm.fr

various amino acids as nitrogen donors for glutamine and nucleotide synthesis (Tsai *et al*, 2021). Indeed, the characteristic metabolic plasticity of PDA can limit the effectiveness of targeting some metabolic dependencies. For example, pancreatic cancer cells are sensitive to inhibitors of glutamine metabolism *in vitro*, but adapt to glutaminase inhibitors when grown as PDA tumors in mouse models (Biancur *et al*, 2017). In line with this, recent screens have compared the metabolic dependencies of PDA tumor cells *in vivo* and *in vitro* and thereby highlighted the importance of select metabolic pathways in the PDA pathophysiologic context and that could constitute relevant therapeutic metabolic targets (Biancur *et al*, 2021; Zhu *et al*, 2021).

Given the high metabolic demand of PDA tumor cells, numerous studies have explored the use of nutrient-deprived diets as a potential anti-carcinogenic approach. The ketogenic diet, which is used to treat epileptic patients (Kessler *et al*, 2011), is a low carbohydrate, low protein, and high fat diet that induces an increase in circulating ketone bodies (KB) (acetooacetate (AcAc) and β -hydroxybutyrate (β OHb)) that are produced largely by hepatocytes from fatty acids. The rationale for the use of the KD stems from the high glycolytic activity of many tumor cells that, upon KD exposure, may experience a metabolic crisis from diet-induced reductions in blood glucose and insulin levels. This diet has been proposed a potential cancer therapy, especially for brain, digestive, or breast cancers (Weber *et al*, 2020). However, given the metabolic heterogeneity of cancers, some tumor cells express ketolytic enzymes that allow them to degrade KB. This metabolic ability was highlighted in hepatocarcinoma cells that adapt to nutrient deprivation and express the ketolytic enzyme SCOT1 (succinyl-CoA:3-oxoacid-CoA transferase encoded by OXCT (3-oxoacid-CoA transferase) 1) to support proliferation (Huang *et al*, 2016). Moreover, in melanoma cells, upregulation of the ketogenic enzyme HMG-CoA lyase (HMGCL), which converts 3-hydroxy-3-methylglutaryl-CoA (HMG-CoA) to AcAc and acetyl-CoA, induces activation of the MEK1/ERK1 axis by AcAc and thereby promotes the growth of BRAF-mutated tumors (Kang *et al*, 2015). However, the metabolic effects of KB on PDA have been less studies, and understanding KB metabolism in tumors with high metabolic flexibility such as PDA is important to understand the

consequences of dietary interventions like the KD which may increase the availability of this nutrient to tumors.

Here, we report that β OHb can contribute to PDA cancer cell metabolism, and that pancreatic tumors express high levels of KB metabolic enzymes. *In vitro*, we show that PDA cells require HMGCL to migrate, invade, and aggregate into tumor spheres. Finally, using PDA murine models, we provide evidence that HMGCL and KB can be required for PDA tumor growth and metastatic invasion.

Results

β OHb contributes to pancreatic tumor aggressiveness and is metabolized by PDA cells

To explore the role of KB on PDA progression, we examined the consequences of intraperitoneal (IP) injection of β OHb in spontaneous PDA bearing Pdx1-Cre; Ink4a/Arf^{f/f}; LSL-Kras^{G12D} (KIC) mice. KIC mice were daily treated with β OHb (100 mg/kg) or vehicle (NaCl 0.9%), starting at 5 weeks of age, and continued for 3 weeks. We observed that β OHb increased pancreatic tumor weight (Fig 1A) and proliferative index (Fig EV1A) without impacting tumor grade (Fig EV1B). We confirmed the growth promoting effects of β OHb on murine pancreatic tumor cells derived from PDA of KIC mice (namely PK4A cells) (Guillaumond *et al*, 2013) when cultured as tumor spheroids and organoids, and clinically validated these data using human PDA tumor cell-derived organoids (Fig 1B and C). Interestingly, β OHb treatment increased staining for monocarboxylate transporters 2 (MCT2) and sodium MCT1 (SMCT1) in β OHb-treated compared to NaCl-treated tumors (45.8% vs. 20.9% and 42.6% vs. 15.6% staining area for MCT2 and SMCT1, respectively) (Fig 1D and E). MCT2, as part of the MCT 1–4 family, and SMCT1 are both MCTs known to transport KB (Martin *et al*, 2006; Perez-Escuredo *et al*, 2016; Huang *et al*, 2017; Li *et al*, 2021), and together with known high expression of MCT1 and MCT4 in PDA (Guillaumond *et al*, 2013), these data suggest that PDA cells have the capacity to take up KBs in tumors. Importantly, we observed more

Figure 1. β OHb promotes PDA aggressiveness.

- A Tumor weight in KIC mice treated with β OHb (100 mg/kg/day, i.p.) or 0.9% NaCl (i.p.) ($n = 13$ mice for NaCl and $n = 15$ mice for β OHb). Data are expressed as mean \pm SEM. Significance was defined by Mann–Whitney test. * $P < 0.05$.
- B Kinetic of spheroid area from PK4A cells cultured during 12 days in medium alone (untreated) or with β OHb 1 or 10 mM ($n = 4$, and 5 respectively). Data are expressed as mean \pm SEM. Significance compared to untreated cells was defined by two-way ANOVA followed by a Dunnett's multiple comparisons test. ** $P < 0.01$, *** $P < 0.0001$.
- C Representative images of mouse PDA and human PDA primary cells-derived organoids after 7 days of culture in medium alone (untreated) or supplemented with 1 or 10 mM of β OHb. Scale bar: 1000 μ m.
- D, E Immunostaining of MCT2 and SMCT1 in tumors of KIC mice treated with β OHb (100 mg/kg/day, i.p.) or 0.9% NaCl (i.p.) ($n = 5$ mice/group). Areas of MCT2 (upper panel) and SMCT1 (lower panel) stainings (D) are expressed as mean of percentage of total tissue area \pm SEM. Significance was defined by Mann–Whitney test. * $P < 0.05$, ** $P < 0.01$. Representative images of MCT2 and SMCT1 stainings (E) in tumors from KIC mice treated with β OHb or NaCl. Scale bar: 100 μ m.
- F Histological characterization of liver and spleen of KIC mice treated with β OHb (100 mg/kg/day, i.p.) or 0.9% NaCl (i.p.) ($n = 14$ mice/group). Number of mice displaying metastatic liver or spleen in each experimental group is reported.
- G Schematic showing isotopomer transition from [U -¹³C] β OHb to label TCA-cycle intermediates, glutamate, and proline. Gray filled circles indicate ¹³C carbon derived from labeled β OHb. Empty circles illustrate unlabeled ¹²C-species.
- H [U -¹³C] β OHb tracing into the TCA intermediate: citrate in poorly differentiated PDA explants from KIC mice ($n = 5$). Data are expressed as mean \pm SEM.
- I Schematic showing ketone metabolism pathway (left panel). Reversible enzymes involved in the production of acetyl-CoA, acetoacetyl-CoA, acetoacetate, β OHb, mT, SCOT1/2, and BDH1/2 are indicated in bold case. Immunoblots of ketone metabolic enzymes (BDH1/2, SCOT1/2, mT) (right panel) in pancreatic tissues from 7-week-old KI ($n = 3$ for BDH1/2, SCOT1/2, and $n = 4$ for mT) and KIC mice ($n = 4$).

Source data are available online for this figure.

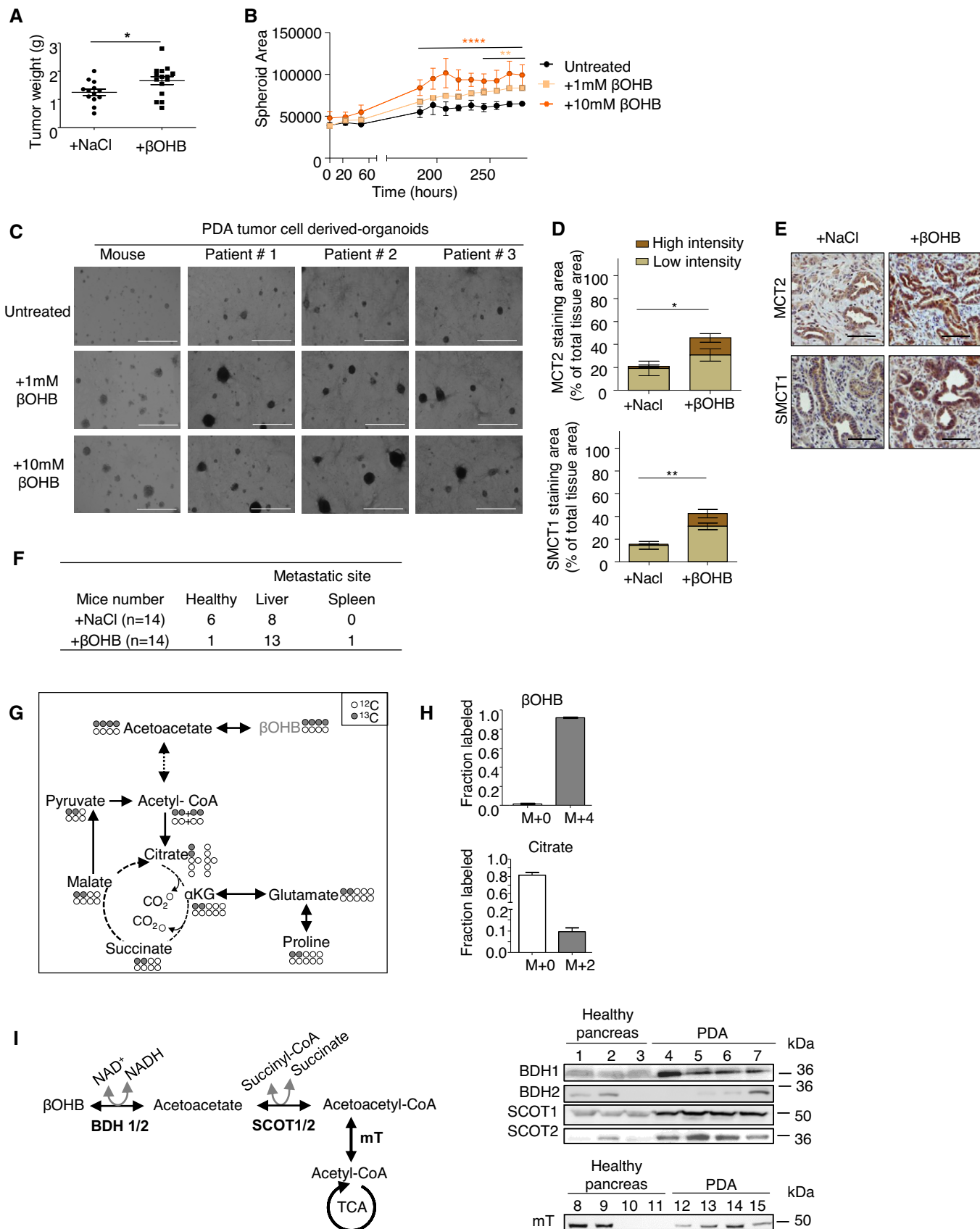


Figure 1.

metastatic lesions in livers from β OHB-treated compared to NaCl-treated PDA-bearing mice (13 vs. 8 mice presented metastatic lesions) suggesting that β OHB promote liver metastases (Fig 1F). In addition, one of 14 β OHB-mice presented evidence of spleen metastases. Altogether these data demonstrate that β OHB promote PDA aggressiveness and metastasis formation.

To determine how β OHB carbons contribute to PDA cell metabolism, we next traced the metabolic fate of U- 13 C-labeled β OHB (Fig 1G) in PDA cells when cultured under decreasing glucose concentrations. Interestingly, some carbon from β OHB was incorporated into TCA cycle metabolites (citrate, α -ketoglutarate (α KG), succinate, malate) as well as glutamate and proline even when high levels of glucose were present (Fig EV1C and Appendix Fig S1A and B). Complete glucose limitation was associated with both increased labeling and decreased levels of these metabolites across several metabolites. These data are consistent with previous work showing that pancreatic cancer can catabolize other fuels for cell survival when glucose is limiting (Gouirand & Vasseur, 2018). We next evaluated the metabolism of β OHB in well-differentiated PDA from 7-week-old KIC mice and in late stage 9-week-old KIC mouse-derived poorly differentiated tumors, which exhibit extensive desmoplasia, by tracing U- 13 C-labeled β OHB in the tumors *ex vivo*. Importantly, and consistent with *in vitro* data, we observed labeling from β OHB-derived carbon in TCA intermediates as well as glutamate and proline in later stage PDA tumors (Figs 1H and EV1D and Appendix Fig S1C and D). Interestingly, we observed the same labeling pattern from β OHB in TCA intermediates, glutamate and proline in well-differentiated tumors, suggesting that KBs can be metabolized by earlier stage tumors as well (Appendix Fig S1E and F). For terminal oxidation of β OHB, PDA cells rely on the expression of several enzymes that are essential for ketolysis (Fig 1I, left panel). We therefore examined levels of a subset of these enzymes in PDA from KIC mice, specifically BDH1/2 (β OHB dehydrogenase 1/2), SCOT1/2, and mT (mitochondrial thiolase encoded by at least ACAT (acetyl-CoA acetyltransferase) 1). Except for BDH2, we found robust over-expression of all enzymes examined in tumors relative to healthy pancreatic tissues (Fig 1I, right panel). Importantly, using histological analysis, we observed that all these KB metabolic enzymes are mainly expressed in tumor gland-like structures (Fig EV1E). Together, these data show that PDA tumor cells express required ketolytic enzymes to metabolize KB.

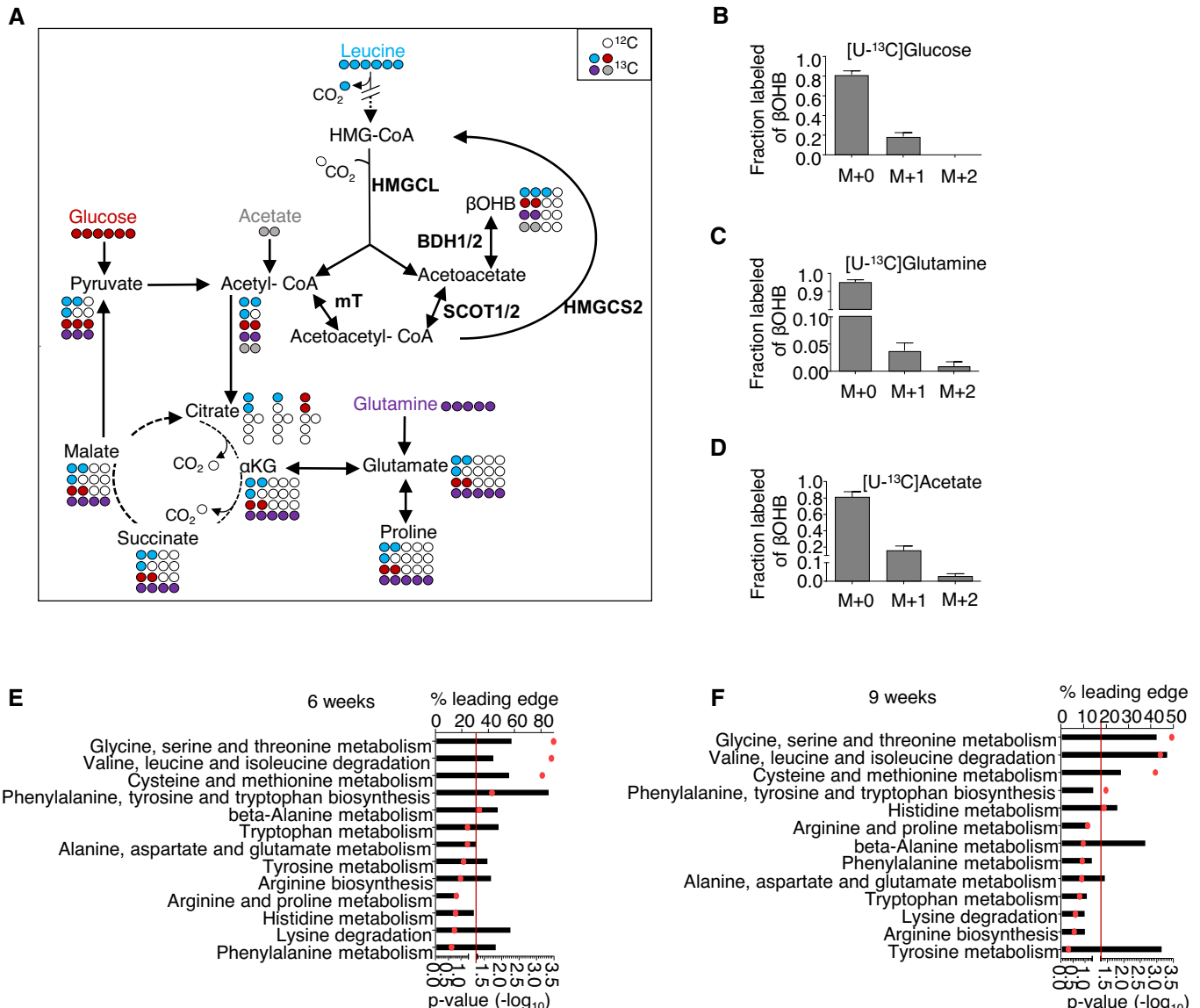
PDA can produce KB from various nutrient sources

As PDA cells are able to use glucose, glutamine, and other carbon sources to support the TCA cycle, we next examined the ability of PDA to produce β OHB from glucose, glutamine, and acetate. We found that a minimal amount of labeled carbon from U- 13 C-glucose, -glutamine and -acetate can be detected in β OHB in *ex vivo* PDA tumors (Fig 2A-D). In line with this, we found that PDA expresses the ketogenic enzymes HMGCL/L1 and HMG-CoA synthase 2 (HMGCS2) in the tumor glands (Fig EV2A-D), in addition to the reversible enzymes SCOT1/2 and mT (Fig 1I). To further explore whether PDA could use other amino acids as carbon sources to produce β OHB, we examined expression of genes coding for enzymes and transporters involved in amino acid metabolism that were differentially expressed between pancreatic tumors at early and late stages of development and age-matched healthy pancreas. Specifically, we

established the transcriptomes of pancreas from control mice (Ink4a/Arf^{f1/f1}; LSL-Kras^{G12D} (KI)) and of pancreas from KIC mice at 6 and 9 weeks of age (Guillaumond *et al*, 2015; Appendix Fig S2A). Using gene set library from the Kyoto Encyclopedia of Genes and Genomes (KEGG) pathway database, we identified genes related to amino acid metabolism (469 genes, 2.15% among all genes) and by a Gene Set Enrichment Analysis (GSEA) those with altered expression in tumors from 6-week-old or 9 week-old PKI mice (205 genes, 0.94% among all genes; and 120 genes, 0.55% among all genes, respectively) compared to control pancreas from age-matched KI mice (Fig EV2E). Among the amino acid metabolic genes deregulated in tumors, we identified, using the percentage of leading-edge genes, the BCAA pathway gene set as among the most significantly deregulated compared to control pancreas with a progressive enrichment for this pathway when the tumor becomes undifferentiated and anaplastic (43.6% vs. 47.3% in PDA from 6-week-old vs. 9-week-old PKI mice, respectively; Fig 2E and F, Appendix Table S1). We next examined expression profiles of genes coding for metabolic enzymes or transporters of leucine, isoleucine, and valine and expanded our analysis to KB metabolic genes. Interestingly, we observed a large diversity of genes with altered expression that code for enzymes involved in leucine breakdown towards HMG-CoA (*Bcat1/2*, *Bckdha/b*, *Mccc1/2*, *Ivd*, *Auh*) and that catalyze the common last step of leucine degradation and KB production (*Hmgcl/l1*), for the reversible enzyme mT (*Acat1*), and for leucine, branched-chain ketoacids and KB transporters (*Slc7a5*, *Slc16a1*, *Slc16a7*) (Fig EV2F, Appendix Table S2). Analysis of BCAT1 expression (BCAA transaminase, which catalyzes the first step of BCAAs degradation) revealed increased levels of this enzyme in PDA as well as its localization in the tumoral compartment (Fig EV2G) as observed for other KB metabolic enzymes. To assess whether the ketogenic BCAA leucine may be used by PK4A PDA-derived tumor cells to support β OHB synthesis, the fate of U- 13 C-labeled leucine was assessed in PK4A cells at various glucose concentrations. This analysis revealed that cells take up leucine similarly regardless of media glucose concentration and that some leucine-derived carbons can be incorporated into citrate, α KG, succinate, malate, pyruvate, glutamate, and proline with increased labeling under glucose restricted conditions (Fig EV2H and Appendix Fig S2B) and that is associated with a drop in levels of these metabolites (Appendix Fig S2C). Interestingly, we found that leucine carbon also could contribute to the β OHB pool in these cells (Fig EV2I and Appendix Fig S2B). We next cultured these cells in conditions where leucine was absent and found that leucine deprivation drastically reduced PK4A cell proliferation. Moreover, addition of β OHB partly rescued proliferation of leucine-starved cells, suggesting that PDA cells can use KB to support proliferation for at least the short term when extracellular leucine is absent (Fig EV2J).

Disruption of HMGCL impedes oncogenic properties of pancreatic tumor cells

Given that PDA cells actively metabolize KB, and KB can promote tumor growth, we questioned whether inhibiting KB metabolism in PDA cells might affect their oncogenic properties. We specifically investigated the effects of disrupting HMGCL, the key enzyme upstream of β OHB synthesis, which in addition to being highly expressed in murine PDA, was found to be up-regulated in human

**Figure 2.** PDA can produce KB.

- A Schematic showing isotopomer transition from [^{13}C]Glucose, [^{13}C]Glutamine, [^{13}C]Acetate, or [^{13}C]Leucine to label TCA-cycle intermediates, glutamate, and proline. Red, violet, gray, and blue filled circles indicate ^{13}C carbon derived from labeled glucose, glutamine, acetate and leucine, respectively. Empty circles denote ^{12}C -species.
- B–D [^{13}C]Glucose ($n = 3$ mice) (B), [^{13}C]Glutamine ($n = 5$ mice) (C) and [^{13}C]Acetate ($n = 6$ mice) (D) tracing into βOHB in poorly differentiated PDA explants from KIC mice. Data are expressed as mean \pm SEM.
- E, F Percentages of leading-edges amino acid genes in 6 weeks (E) or 9 weeks (F) KIC mice as compared to age-matched KI mice that contribute to the GSEA enrichment. Red spots represent the P -value of the deregulated amino acid pathways in KIC mice as compared to KI mice. Red line corresponds to a P -value of 0.05.

Source data are available online for this figure.

PDA (Fig EV3A). The contribution of HMGCL to tumor progression other than PDA has been suggested to be cancer-type and stage specific (Saraon *et al*, 2013), (Luo *et al*, 2017). In PDA, little is known about the role of HMGCL in tumor cell proliferation, migration, and invasion. We generated clonal populations of sg-HMGCL PANC-1 cells (sg-HMGCL) in which HMGCL expression was completely abolished (in clones #2–6) as compared to sg-Control PANC-1 cells

(sg-CTRL) (Appendix Fig S3A). HMGCL disruption did not impact PANC-1 cell proliferation (P -value > 0.05 ; Appendix Fig S3B and C) but prevented the clonogenic capacity of the cells (Fig 3A, Appendix Fig S3D). Using wound healing assays and transwell migration or invasion chambers, we found that HMGCL disruption drastically decreased the migratory potential of PDA cells (Fig 3B and C, Appendix Fig S3E) and also affected their invasive behavior

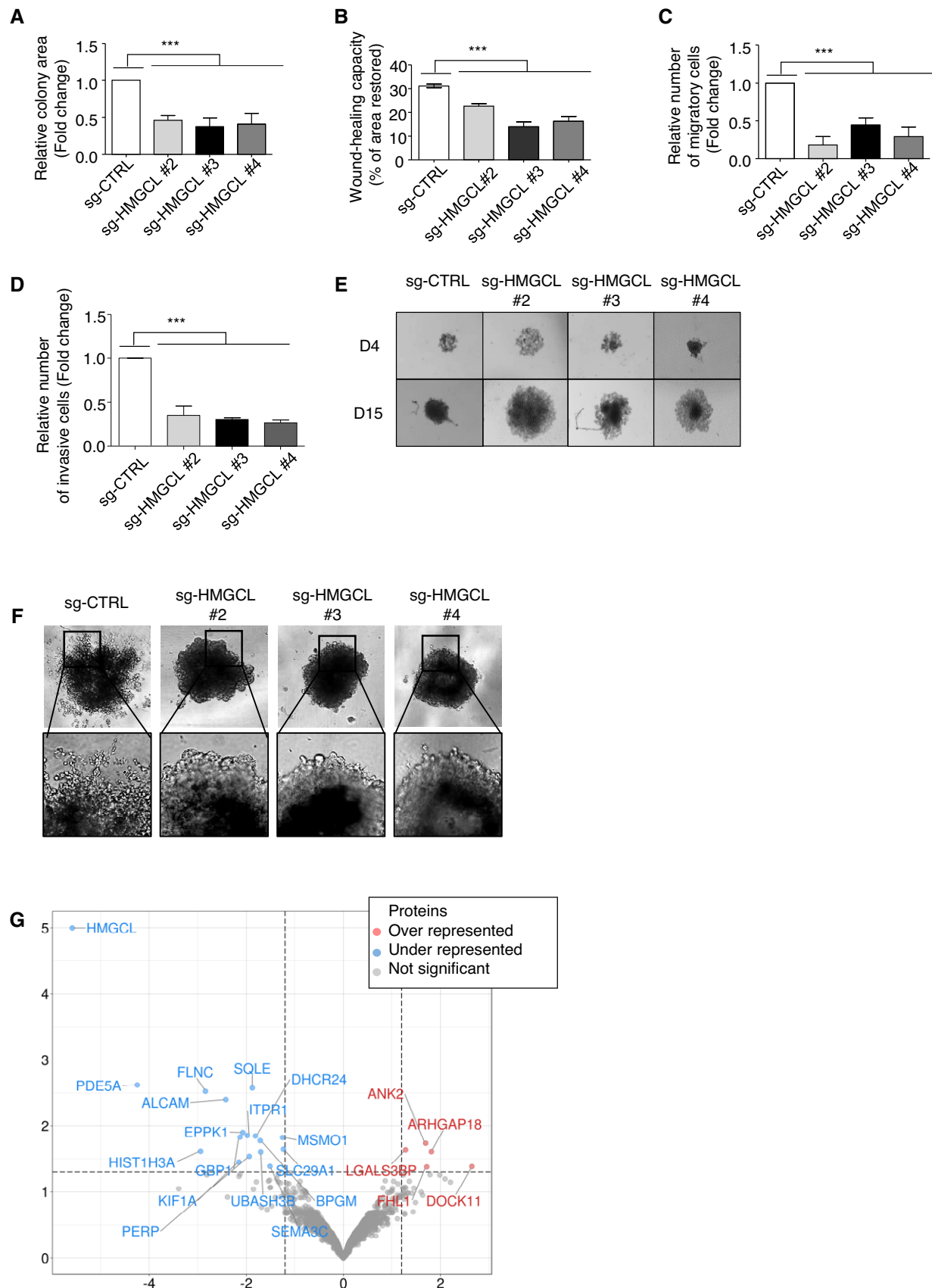


Figure 3.

Figure 3. HMGCL targeting limits oncogenic properties of pancreatic tumor cells.

- A Quantification of colony forming area of sg-CTRL and sg-HMGCL (#2, #3 and #4 clones) PANC-1 cells. Colony area is expressed as mean fold change relative to sg-CTRL ± SEM ($n = 3$ independent experiments). Significance was defined by one-tailed Student's t-test. *** $P < 0.001$.
- B Quantification of wound healing capacity of sg-CTRL and sg-HMGCL (#2, #3 and #4 clones) PANC-1 cells. Wound healing capacity is expressed as mean of percentage of restored area at 72 h ± SEM ($n = 4$ independent experiments). Significance was defined by one-tailed Student's t test. *** $P < 0.001$.
- C, D Quantification of migratory (C) and invasive (D) sg-CTRL and sg-HMGCL (#2, #3 and #4 clones) PANC-1 cells. Migratory or invasive cell numbers are expressed as mean fold change relative to sg-CTRL cells ± SEM ($n = 3$ independent experiments). Significance was defined by one-tailed Student's t test. *** $P < 0.001$.
- E Representative images of spheroid formation from sg-CTRL and sg-HMGCL (#2, #3 and #4 clones) PANC-1 cells after 4 or 15 days of culture. Photos are representative of $n = 3$ independent experiments.
- F Representative images of spheroid invasion assay from sg-CTRL and sg-HMGCL (#2, #3 and #4 clones) PANC-1 cells after 10 days of culture in presence of Matrigel. Photos are representative of $n = 3$ independent experiments.
- G Volcano plot illustrating proteins significantly under- or over-represented in sg-CTRL and sg-HMGCL PANC-1 spheroids ($n = 3$ independent experiments). Significance was defined by one-tailed Student's t-test. Protein levels with a q -value < 0.05 (horizontal axis) and a fold change < -1.5 or $> +1.5$ (vertical axis) are considered as significantly down or up-regulated in sg-HMGCL PANC-1 spheroids.

Source data are available online for this figure.

(Fig 3D). We confirmed in MiaPaCa-2 human PDA cells, which also express significant amounts of HMGCL, that inhibition of HMGCL does not impact proliferation but impedes clonogenic and migratory potential (Appendix Fig S3F–I). In three dimensions, when cultured under anchorage-independent conditions, although sg-HMGCL and sg-CTRL PANC-1 had the same proliferation index, sg-HMGCL PANC-1 spheroids were larger, indicating that HMGCL disruption impeded proper aggregation of PDA cells when cultured as spheroids (Fig 3E, Appendix Fig S3J and K). Interestingly, HMGCL silencing also abolished the invasive abilities of PANC-1 spheroids (Fig 3F). We further compared the proteome of sg-CTRL and sg-HMGCL PANC-1 cells to identify changes in protein expression associated with loss of 3D-associated oncogenic features following HMGCL disruption. Among downregulated proteins upon HMGCL loss, we identified ALCAM, SEMA3C, FLNC, and GBP1/3 involved in tumor cell migration, invasion, cell-to-cell adhesion, and cytoskeleton homeostasis (Bagci *et al*, 2009; Li *et al*, 2017; Honkala *et al*, 2019; Kamil *et al*, 2019; Ni *et al*, 2021), and SQLE, MSMO1, and DHCR24 that belong to sterol metabolism (Fig 3G, Appendix Table S3). In line with this proteomic data, we validated decreased levels of ALCAM and several of its targets (namely EPHA2, FLNB, PLA2U), and of SEMA3C and SQLE following HMGCL silencing (Fig EV3B–D). Interestingly, ALCAM positively regulates cell

adhesion, migration, and invasion of endometrial cancer cells (Devis *et al*, 2017), and SQLE, a rate-limiting enzyme in the cholesterol biosynthesis pathway, promotes invasiveness of hepatocellular carcinoma (Sui *et al*, 2015) and tumor aggressiveness in breast cancer patients (Kim *et al*, 2021). Indeed, we observed that increased expression of ALCAM and SQLE in sg-HMGCL PANC-1 cells (Appendix Fig S3L and M, and Fig EV3E) does not alter cell proliferation (Appendix Fig S3N) but does restore the ability of these cells to migrate (Fig EV3F and G) and to form well-aggregated spheroids (Fig EV3H) with invasive capacities (Fig EV3I). Collectively, these data show that HMGCL is dispensable for pancreatic cancer cell proliferation but supports their aggressive, invasive phenotype as well as their migratory abilities *in vitro*.

HMGCL and βOHB contribute to pancreatic tumor aggressiveness

To examined the role of HMGCL on PDA progression, we orthotopically injected sg-HMGCL PANC-1 cells or sg-CTRL cells into nude mice. HMGCL depletion impeded tumor growth as demonstrated by a decrease in size and weight of sg-HMGCL tumors compared to control tumors (Fig 4A and B). Moreover, in these tumors we observed a reduced stromal content compared to sg-CTRL tumors (Fig 4C). We next assessed the effect of βOHB administration on

Figure 4. HMGCL and βOHB promote pancreatic tumor aggressiveness.

- A, B Quantification of volume with representative images (A) and weight (B) of sg-CTRL ($n = 15$ for A and $n = 9$ for B), sg HMGCL #2 ($n = 19$ for A and $n = 8$ for B), #3 ($n = 7$ for A and B) pancreatic tumors. Data are expressed as mean of tumor volume or weight ± SEM. Significance was defined by Mann–Whitney test. * $P < 0.05$, ** $P < 0.01$, *** $P < 0.001$.
- C Extracellular matrix quantification following trichrome staining in sg-CTRL and sg-HMGCL #2 pancreatic tumors sections ($n = 8$ and 9 mice/group respectively, left panel). Data are expressed as mean of percentage of total tissue area ± SEM. Significance was defined by Mann–Whitney test. ** $P < 0.01$. Representative images of trichrome staining in sg-CTRL and sg-HMGCL pancreatic tumors. Scale bar: 100 μm (right panel).
- D, E Quantification of volume (D) and weight (E) of sg-CTRL pancreatic tumors treated with 0.9% NaCl (i.p.) ($n = 4$), and pancreatic tumors from two different clones of sg-HMGCL treated with 0.9% NaCl (i.p.) or βOHB (100 mg/kg/bi-weekly, i.p.) ($n = 10$ /group). Data are expressed as mean of tumor volume or weight ± SEM. Significance was defined by Mann–Whitney test. ns: not significant, ** $P < 0.01$.
- F Histological characterization and representative picture of liver from mice orthotopically xenografted with sg-CTRL or sg-HMGCL PANC-1 cells and treated with 0.9% NaCl (i.p.) or βOHB (100 mg/kg/bi-weekly, i.p.). Number of mice displaying healthy or metastatic liver in each experimental group is reported. Metastatic area (orange star) is separated from liver (green circle) by dotted lines. Scale bar: 100 μm (inset images scale bar: 20 μm).
- G Schematic showing isotopomer transition from [$U-^{13}\text{C}$]βOHB to label TCA-cycle intermediates, glutamate, and proline. Gray filled circles indicate ^{13}C carbon derived from labeled βOHB. Empty circles illustrate unlabeled ^{12}C -species.
- H [$U-^{13}\text{C}$]βOHB tracing into TCA intermediate: citrate in sg-CTRL and sg-HMGCL #2 and #3 PANC-1 cells cultured in indicated glucose concentrations. Data are expressed as mean ± SEM ($n = 2$ independent experiments). Significance was defined by one-way ANOVA followed by a Bonferroni's multiple comparisons test, only significances between sg-HMGCL #2, #3 PANC-1 cells and sg-CTRL PANC-1 cells under the same culture condition are mentioned. *** $P < 0.001$.

Source data are available online for this figure.

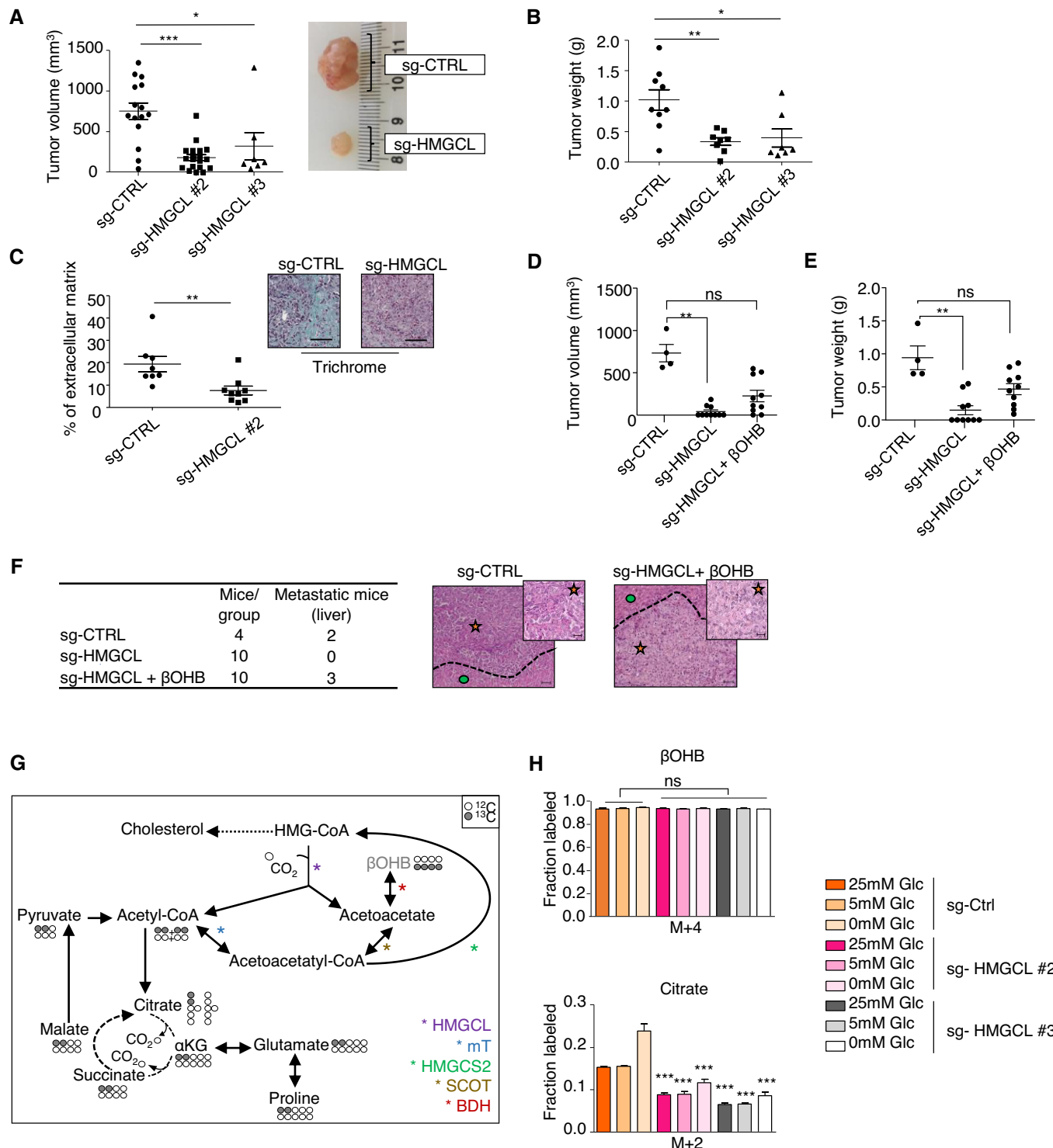


Figure 4.

tumor growth when given twice a week beginning 7 days after orthotopic injections of sg-HMGCL PANC-1 cells. Although providing βOHB did not restore tumor growth to the same levels as sg-CTRL tumors, βOHB administration significantly increased size and weight of sg-HMGCL tumors (Fig 4D and E and Appendix Fig S4A) and liver metastasis incidence in sg-HMGCL tumor-bearing mice

(Fig 4F and Appendix Fig S4B). We next assessed βOHB fate in conditions of HMGCL disruption to examine the consequences of HMGCL deficiency on the ability of PDA cells to metabolize exogenous βOHB . We found that the contribution of βOHB to TCA intermediates, glutamate, and proline was less in these conditions than in control cells (Figs 4G and H, and EV4A and Appendix Fig S4C).

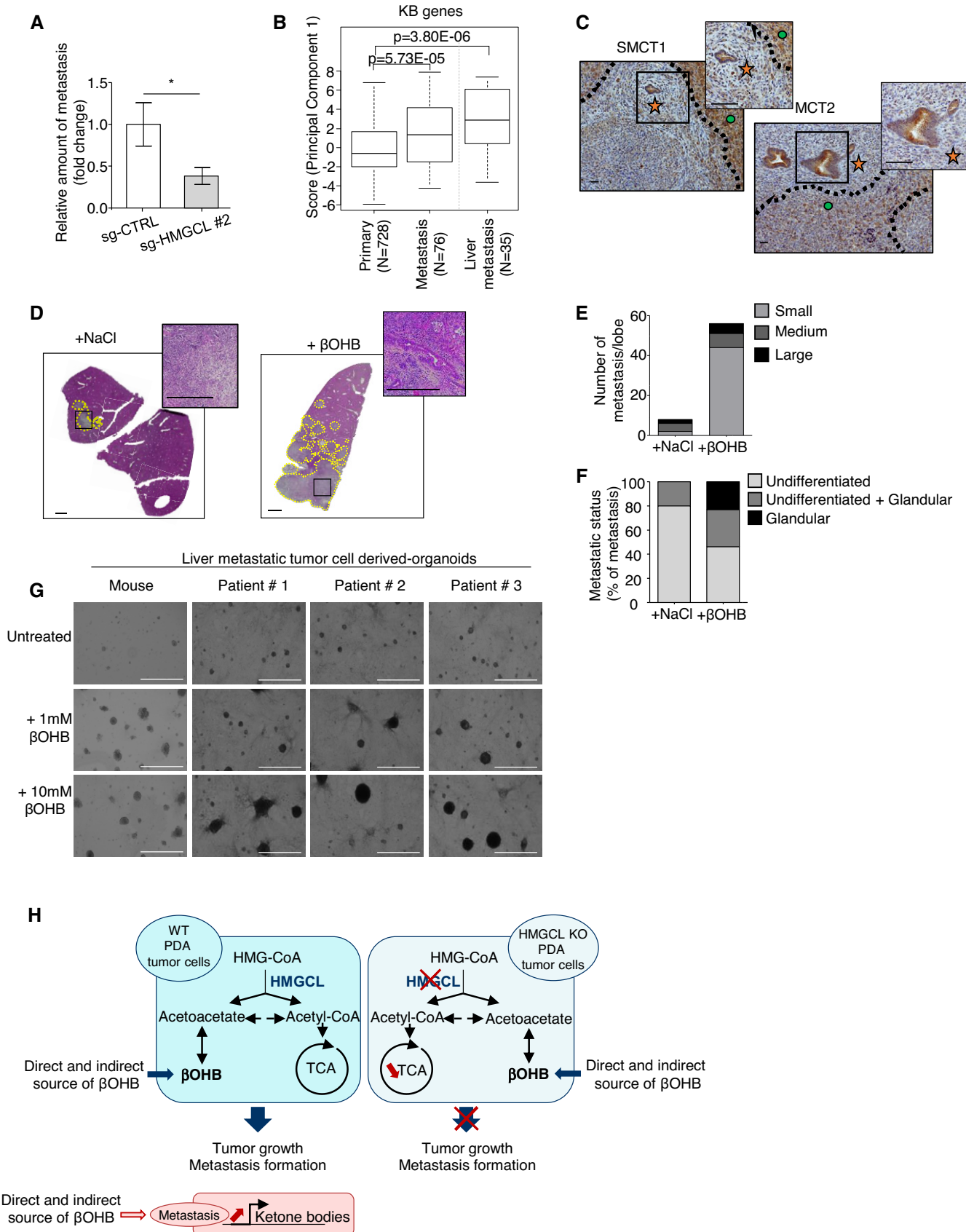


Figure 5.

Figure 5. HMGCL and βOHB favor metastatic dissemination of PDA cells.

- A Human ALU sequences quantification in lower chorioallantoic membrane (CAM) of chicken embryo injected with sg-CTRL or sg-HMGCL #2 PANC-1 cells. Relative amount of metastasis is expressed as mean fold change relative to sg-CTRL \pm SEM ($n = 8$ /group). Significance was defined by one-tailed Student's t-test. * $P < 0.05$.
- B Box-and-whisker plots of ketone bodies (KB) metagene score defined as first component of PCA of genes in primary tumors ($n = 728$), in all metastases ($n = 76$), and in liver metastases specifically ($n = 35$). Box-and-whisker plot were defined with default parameters by median value (central band at the 50th percentile), interquartile ranges (IQR, box limited by 25th and 75th percentile) and whisker boundaries defined at 1.5 \times IQR. Significance was defined by Student's t-test.
- C Representative immunostaining of SMCT1 and MCT2 in metastatic livers of KIC mice ($n = 3$ mice). Metastatic area (orange star) is separated from liver (green circle) by dotted lines. Scale bar: 100 μ m.
- D–F Effect of βOHB treatment on liver metastatic incidence, size and status. Representative HPS staining of liver lobes from metastatic mice treated with βOHB (100 mg/kg/day, i.p.) or 0.9% NaCl (i.p.) ($n = 8$ mice/group). Metastatic areas are separated from liver by yellow dotted lines. Scale bar: 1 mm and 500 μ m for insets (D). Number and size of metastasis per lobe and classified in small, medium, and large size (E). Pathological status of metastasis from mice treated with βOHB or NaCl ($n = 13$ or 5 lobes/group, respectively). Data are expressed as percentage of total metastasis in all liver lobes presenting metastasis (F).
- G Representative images of mouse and human liver metastatic cells-derived organoids after 7 days of culture in medium alone (untreated) or supplemented with 1 or 10 mM of βOHB. Scale bar: 1,000 μ m.
- H Working model: HMGCL and βOHB promote pancreatic tumor expansion and dissemination. PDA tumor cells expressed HMGCL (left panel). In this setting, PDA can use βOHB from direct source as tumor surrounding βOHB, mimicked in our study by direct injection of βOHB, and indirect source from degradation of various nutrients. βOHB and HMGCL contribute to tumor growth and metastases formation. In metastases, ketone bodies genes are upregulated. When HMGCL is knockout (right panel), contribution of βOHB in TCA cycle is reduced and tumor growth as well as dissemination capacity of PDA tumor cells are strongly disturbed.

Source data are available online for this figure.

While it is unclear how loss of HMGCL affects metabolism of exogenous βOHB, these data may explain why providing βOHB does not fully rescue HMGCL loss in regards with tumor growth. Importantly, there was no change in glucose or glutamine consumption between sg-CTRL and sg-HMGCL PANC-1 cells, and glucose and glutamine consumption is unchanged by βOHB treatment, suggesting that glucose and glutamine uptake is not affected by HMGCL disruption and/or βOHB supplementation in PDA cells (Appendix Fig S4D and E). βOHB is catabolized to acetoacetyl-CoA which is further converted either by mT to acetyl-CoA for terminal oxidation into the TCA cycle or is potentially rewired towards HMG-CoA production by HMGS2. The decreased catabolism of βOHB to TCA intermediates in sg-HMGCL cells led us to ask whether βOHB was preferentially converted to HMG-CoA, which might contribute to cholesterol (Fig 4G). We found that a contribution of βOHB carbon to cholesterol synthesis was decreased in sg-HMGCL PANC-1 compared to sg-CTRL PANC-1 (Fig EV4B). This inability of HMGCL-depleted PANC-1 cells to use βOHB for cholesterol synthesis could be explained by decreased levels of SQLE, MSMO1, and DHCR24, three enzymes of the sterol arm of the cholesterol biosynthesis pathway (Fig 3G). Taken together, these data suggest that HMGCL is important for PDA tumor growth and that exogenous βOHB can partly compensate lack of HMGCL without totally recapitulating growth and metabolism of HMGCL-expressing PDA cells.

HMGCL and βOHB favor metastatic dissemination of PDA cells

To assess whether HMGCL supports the metastatic potential of cancer cells *in vivo*, we performed an *in ovo* assay by inoculating sg-CTRL and sg-HMGCL PANC-1 cells onto chick-embryo chorioallantoic membranes (CAMs). CAM is a supportive environment to evaluate the PDA metastatic potential (Hagedorn *et al*, 2005) (Dumartin *et al*, 2010) (Mikaelian *et al*, 2013). After 10 days of PANC-1 cell engraftment on the upper CAM, we monitored metastasis formation by evaluating the presence of tumor cells at the lower CAM that had migrated through the vicinity of preexisting vessels and disseminated to distant sites. We observed that in the absence of HMGCL the metastatic potential of PANC-1 cells was reduced as compared

to HMGCL expressing PANC-1 cells (Fig 5A). In PDA patients, primary pancreatic tumor cells preferentially disseminate to the liver (76–94%), compared to peritoneum (41–56%), abdominal lymph nodes (41%), and lungs (45–48%) (Makohon-Moore *et al*, 2017). To determine whether ketone metabolism was associated with metastasis in PDA patients, we examined expression of 15 KB metabolism genes in 728 primary pancreatic carcinoma samples and 76 metastatic samples (mainly liver and peritoneal sites) extracted from 15 publicly available whole-genome mRNA expression data sets (Appendix Table S4). We defined a global measurement of the 15 KB metabolism genes using a metagene approach in which the KB-related metagene was computed as the first component of a principal component analysis (PCA). The comparison between metastatic vs primary tumor samples showed higher expression of the KB metagene score in metastases than in primary tumors (Fig 5B, Appendix Table S5). Interestingly, KB genes expression is robustly increased in liver metastases compared to PDA as illustrated for *Hmgcl*, *Hmgcs2*, *Bdh1*, and *Slc16a1* (Fig EV5). Moreover, immunostaining of KB transporters in liver metastasis of PDA-bearing KIC mice revealed the presence of SMCT1 and MCT2 in tumor cells within liver metastasis (Fig 5C, and Appendix Fig S5A). These data, combined with the increased liver metastatic index of βOHB-treated PDA-bearing mice (Figs 1F and 4F), suggested that PDA cells, when established in liver, have the ability to use KB. To test this hypothesis, we developed a mouse model of induced-liver metastasis (I-LM) and implanted PK4A cells into the liver of syngenic healthy KI mice. The same number of tumor cells was implanted into two separate liver lobes for all mice. Three days after cell engraftment, mice were treated with βOHB for 10 days and then sacrificed for examination of liver metastasis. Although macroscopic liver metastases were observed in both vehicle control- and βOHB-treated groups (Appendix Fig S5B), histological analysis of livers revealed more numerous tumors in βOHB-treated as compared to NaCl-treated mice (Fig 5D). PK4A cells implanted in livers of vehicle-treated mice formed fewer tumor foci that were localized at the injection site with a negligible number of small disseminated lesions, whereas βOHB treatment promoted colonization of liver lobes by PK4A cells and the appearance of high numbers of small- and medium-sized tumors (Fig 5E).

Moreover, the mice injected with β OHB developed a higher percentage of well-differentiated tumors in liver than that of the mice in the control group (Fig 5F). When I-LM mouse models were submitted to leucine-enriched diet, the examination of liver metastases 10 days after grafts revealed that leucine-enriched diet also promoted metastatic dissemination with an increased number of small and medium metastasis (Appendix Fig S5C–E). Consistent with these *in vivo* data, treatment of mouse or human liver metastatic tumor cell derived-organoids with β OHB promotes their growth (Fig 5G). Collectively, these data support a role for KB as a promoter of PDA metastasis.

In summary, our data demonstrate that β OHB strongly participates in the acquisition of the metastatic phenotype of PDA and that PDA cells can activate KB metabolism. In this context, we show that HMGCL, upstream of β OHB production, supports tumor expansion and PDA cells dissemination (Fig 5H).

Discussion

Pancreatic ductal adenocarcinoma evolution is characterized by a silent, asymptomatic progression phase, followed by a tumor burden that almost inevitably gives rise to a symptomatic aggressive metastatic cancer. Moreover, PDA progression is associated with a massive metabolic reprogramming which supports tumor expansion (Gouirand *et al*, 2018; Vaziri-Gohar *et al*, 2018). Indeed, one of the hallmarks of PDA is its metabolic plasticity that makes this tumor able to grow despite a dense microenvironment as well as an inefficient vascular network which encloses and deprives tumor cells of nutrients and oxygen. This led us to investigate if PDA's ability to activate KB metabolism represents a new facet of PDA metabolic flexibility, as KB represent an alternative fuel in mammals that is particularly prominent in conditions of nutrient stress. Interestingly, concomitant ketogenesis versus ketolysis has been described in the context of breast cancer in cancer-associated fibroblasts versus epithelial tumor cells respectively (Martinez-Outschoorn *et al*, 2012). Ketone oxidation also has been reported in several solid cancers such as brain and liver tumors in which BDH and SCOT enzymes are upregulated (De Feyter *et al*, 2016) (Huang *et al*, 2016; Zhang & Xie, 2017). Hence, it appears that tumor cells derived from multiple organs are able to activate KB metabolism, which may be relevant to whether the use of the KD is effective as an anti-cancer therapy. In the context of PDA, while the KD has been shown to reduce pancreatic tumor growth *in vivo* in some models (Shukla *et al*, 2014), other studies revealed no effect of KD alone on PDA tumor growth or animal survival (Hopkins *et al*, 2018; Lien *et al*, 2021). Moreover, the limited number of PDA patients studied with this dietary intervention and the lack of long-term follow-up make the role of the KD in treating PDA patients unclear (Zhang *et al*, 2021).

In order to directly evaluate the impact of KB on PDA evolution, we examined the effect of β OHB on PDA and found evidence for a direct benefit of ketones on PDA expansion. These findings are consistent with data from a mouse model of spontaneous mammary tumors (Rodrigues *et al*, 2017). In addition, using *in vitro* tracing of β OHB fate, we found that β OHB can be metabolized by PDA cells, particularly when glucose is limiting and that this ketolysis is preserved even in PDA tissue slices containing multiple cell types. Accordingly, expression of the ketolytic enzymes BDH, SCOT, and

mTH in PDA enables SCOT-dependent oxidation of KB, as for liver, breast, prostate, and colon tumors (Martinez-Outschoorn *et al*, 2012; Saraon *et al*, 2013; Huang *et al*, 2016; Lee *et al*, 2016), and is in accordance with its active consumption of KB.

The reversible activity of mT and SCOT as well as their high levels in PDA led us to hypothesize that PDA cells have also the ability to produce their own pool of KB from acetyl-CoA (Fig 4G). A second mechanism of KB production is the HMGCS2-dependent ketogenesis, which is favored in ketogenic organs, such as liver, and has been suggested to occur in other tissues and cells including tumor cells (Grabacka *et al*, 2016). Interestingly, we found that PDA cells express HMGCS2 and HMGCL, which are both required for *de novo* ketogenesis, suggesting that both HMGCS2- and SCOT-dependent ketogenesis may be active in PDA. *Ex vivo*, we showed that some nutrients can contribute carbon to KB production, even though labeling of KB is relatively low from any carbon source. Hence, the dependence of PDA cells on HMGCL suggests that production of KB plays some role. Importantly, loss of HMGCL drastically impacts on PDA growth and aggressiveness and reduces β OHB metabolism via a mechanism still to be determined, which probably explains the partial rescue of HMGCL loss by exogenous KB. This may suggest that a link between ketogenesis and ketolysis that needs to be further explored exists in these cells and underlies how ketone metabolism affects PDA progression. Another HMGCS2-independent ketogenic pathway relies on catabolism of BCAAs. Previous studies have demonstrated that BCAAs are increased in the circulation early during PDA development, with the BCAAs being derived from the increased breakdown of tissue protein (Mayers *et al*, 2014). Although the uptake of BCAAs appears to be low in PDA tumors and the tumors do not require BCAT to grow (Mayers *et al*, 2016), it has been reported that leucine supplementation can still promote pancreatic tumor burden, suggesting that leucine metabolism may still contribute in some way to PDA growth (Liu *et al*, 2014). In mammals under nutrient starvation, catabolism of leucine towards KB is rapid and accounts for approximately 4% of KB supply (Thomas *et al*, 1982). By transcriptomic analysis of PDA, we revealed that enzymes of BCAAs catabolism together with KB metabolic enzymes are commonly up-regulated during tumor progression and tracing of leucine revealed that carbon from this amino acid can also contribute to the β OHB pool. Hence, a contribution of leucine to *de novo* ketogenesis, either in cancer cells or in tissues outside of the cancer, may be one way that this amino acid can promote PDA growth.

A role for HMGCL in cancer is controversial, with both pro- and anti-tumoral effect of this enzyme reported in various cancers (Saraon *et al*, 2013; Kang *et al*, 2015; Luo *et al*, 2017). We find that HMGCL can promote PDA progression and whether HMGCL represents a good cancer target will depend on the cancer context. Ketogenesis as a metabolic process is crucial in specific physiological contexts associated with fasting and starvation periods. Indeed, loss of function of HMGCL is associated with hypoglycemia, acidosis, hyperammonemia, and severe neurological symptoms (Grunert *et al*, 2017). However, the pathogenesis associated with the metabolic crisis caused by congenital HMGCL deficiency is not fully understood, and the enzyme may not be required in all cases in otherwise normal adults. As PDA cells are submitted to nutritional stress, one might suspect that HMGCL plays a more important role in this context. In addition, the proteomic profile of HMGCL

depleted PDA cells revealed alteration of several, so far unsuspected, proteins involved in sterols synthesis such as SQLE, MSOM1, and DHCR24. Hence, HMGCL depletion might slow cholesterol biosynthesis, thereby increasing levels of squalene, a toxic product when accumulated in cells with low levels of SQLE. Such accumulation might provoke alterations in oncogenic functions of

PDA cells, independently of sterol synthesis inhibition, as previously shown for lung neuroendocrine tumors (Mahoney *et al*, 2019). In light of these results, it appears important to further explore the molecular mechanisms regulated by HMGCL that lead to these unsuspected protein alterations in order to validate HMGCL as a druggable candidate to target PDA aggressiveness.

Materials and Methods

Reagents and Tools table

Reagents or Tools	Source	Identifier
Antibodies		
Rabbit Polyclonal Anti-ACAT1 (WB)	Sigma	Cat# AV54278, RRID: AB_1844483
Mouse Monoclonal Anti-ALCAM/CD166 (WB)	Santa Cruz Biotechnology	Cat# sc-74558, RRID : AB_2289495
Mouse Monoclonal Anti-ALCAM/CD166 (FACS)	BD Biosciences	Cat# 559260, RRID:AB_397209
Mouse Monoclonal Anti-β-Actin	Sigma-Aldrich	Cat# A5316, RRID:AB_476743
Rabbit Polyclonal Anti-BCAT1	Aviva Systems Biology	Cat# ARP46132_P050, RRID:AB_10640125
Rabbit Polyclonal Anti-BDH1	Novus Biologicals	Cat# NBP1-88673, RRID:AB_11009202
Rabbit Polyclonal Anti-BDH2	Sigma	Cat# HPA036028, RRID:AB_10670674
Rabbit Polyclonal Anti-Hmgcl	Abcam	Cat# ab197022, RRID:AB_2797140
Rabbit Polyclonal Anti-Hmgcl1	Abcam	Cat# ab101576, RRID:AB_10712203
Rabbit monoclonal Anti-HMGC52 (IHC)	Abcam	Cat# ab137043, RRID: AB_2749817
Rabbit Polyclonal Anti-HMGC52 (WB)	Sigma	Cat# AV41562, RRID: AB_1850800
Rat Monoclonal Anti-Ki67	Biolegend	Cat# 652402, RRID:AB_11204254
Rabbit Polyclonal Anti-SLC16A7/MCT2	Bioss	Cat# bs-3995R, RRID:AB_10855300
Rabbit Polyclonal Anti-OXCT1 (SCOT1)	Novus Biologicals	Cat# NBP1-82462, RRID:AB_11027140
Rabbit Polyclonal Anti-OXCT2 (SCOT2)	Thermo Fisher Scientific	Cat# PA5-49312, RRID:AB_2634766
Rat Polyclonal Human/Mouse anti-Semaphorin 3C	R&D Systems	Cat# MAB1728, RRID:AB_2301533
Rabbit Polyclonal Anti-SQLE	Proteintech	Cat# 12544-1-AP, RRID:AB_2195888
Rabbit Polyclonal Anti-SLC5A8/SMCT1	Bioss	Cat# bs-6106R, RRID:AB_11108966
Goat Polyclonal Anti-Rat IgG - HRP	Santa Cruz Biotechnology	Cat# sc-2006, RRID:AB_1125219
Goat Polyclonal Anti-Mouse IgG Human ads - HRP	Southern Biotechnology	Cat# 1030-05, RRID:AB_2619742
Goat Polyclonal Anti-Rabbit IgG – HRP	Southern Biotechnology	Cat# 4030-05, RRID:AB_2687483
Rabbit Polyclonal Anti-Goat IgG (H + L) – HRP	Southern Biotechnology	Cat# 6160-05, RRID:AB_2796231
Goat Polyclonal Anti-Mouse IgG (H + L) - Alexa Fluor 488	Thermo Fisher Scientific	Cat# A-11029, RRID:AB_138404
Biological Samples		
Healthy pancreas and PDA protein extract from PDA patients	Leca <i>et al</i> (2016)	https://doi.org/10.1172/JCI87734
Chemicals, Peptides, and Recombinant Proteins		
Lipofectamine 3000	Thermo Fisher Scientific	Cat# L3000015
G418	Thermo Fisher Scientific	Cat# 10131027
Mitomycin C	Sigma Aldrich	Cat# 10107409001
Collagenase type V	Sigma Aldrich	Cat# C9263
Critical Commercial Assays		
CellTrace™ CFSE Cell Proliferation Kit	Thermo Fisher Scientific	Cat# C34554
VECTASTAIN ABC kit	Vector	Cat# PK-6100
Liquid DAB and substrate chromogen system	DAKO	Cat# K3468
Corning BioCoat™ Matrigel Invasion Chamber	Corning	Cat# 11553570

Reagents and Tools table (continued)

Reagents or Tools	Source	Identifier
Trichrome Masson kit	RAL DIAGNOSTICS	Cat# 361350-0000
Deposited Data		
9-week RMA data	Guillaumond <i>et al</i> (2015)	GSE61412
6-week RMA data		GSE127891
Experimental Models: Cell Lines		
PK4a mouse cells	Guillaumond <i>et al</i> (2013)	RRID:CVCL_WB21
PANC-1 human cells	ATCC	Cat# CRL-1469, RRID:CVCL_0480
MiaPaCa-2 human cells	ATCC	Cat# CRL-1420 RRID:CVCL_0428
Experimental Models: Organisms/Strains		
Pdx1-Cre; Ink4a/Arf ^{f/f} ;LSL-Kras ^{G12D} mice	Aguirre <i>et al</i> (2003)	https://doi.org/10.1101/gad.1158703
HsdCpb:NMRI-Foxn1nu	Envigo	Cat# 5652667, RRID:MGI:5652667
Oligonucleotides		
36B4 primer Forward AATCCCTGACCGCACGCCGTGATG	Guillaumond <i>et al</i> (2015)	https://doi.org/10.1073/pnas.1421601112
36B4 primer Reverse TGGTTTCCAGGTGCCCTCG	Guillaumond <i>et al</i> (2015)	https://doi.org/10.1073/pnas.1421601112
Filamin B primer Forward AGTTAACGCCAGCATCCT	Devis <i>et al</i> (2017)	https://doi.org/10.1002/path.4851
Filamin B primer Reverse TGACATCGATGGTGTGGACA	Devis <i>et al</i> (2017)	https://doi.org/10.1002/path.4851
Epha2 primer Forward GGCTTCTTATCCACCGCAG	Devis <i>et al</i> (2017)	https://doi.org/10.1002/path.4851
Epha2 primer Reverse CGAGGATGTCTTCAGCATGC	Devis <i>et al</i> (2017)	https://doi.org/10.1002/path.4851
Plau primer Forward TTCAACCACATCGAGAACCA	Devis <i>et al</i> (2017)	https://doi.org/10.1002/path.4851
Plau primer Reverse TTGGTGTGGAGTTAACCC	Devis <i>et al</i> (2017)	https://doi.org/10.1002/path.4851
Recombinant DNA		
HMGCL Crispr/Cas9 KO plasmids	Santa Cruz Biotechnologies	Cat# sc-422425
HMGCL HDR plasmids	Santa Cruz Biotechnologies	Cat# sc-403841-HDR
Control CRISPR/Cas9Plasmid	Santa Cruz Biotechnologies	Cat# sc-418922
pcDNA3.1(+)-N-DYK	GeneScript	/
ALCAM cDNA (pcDNA3.1(+)-N-DYK)	GeneScript	/
SQLE cDNA (pcDNA3.1(+)-N-DYK)	GeneScript	/
Software and Algorithms		
R studio 3.4.4	RStudio, Inc.	RRID:SCR_000432
Gene Set Enrichment Analysis with the fgsea package	Bioconductor	RRID:SCR_003199
Image J	National Institutes of Health	RRID:SCR_003070
Prism Version 5.03	Graph Pad	RRID:SCR_002798
Ingenuity Pathway Analysis	IPA®	RRID:SCR_008653
FlowJo Version 10	FlowJo LLC	RRID:SCR_008520
Other		
DMEM medium without glutamine (Gln-)	Thermo Fisher Scientific	Cat# 11960-044
DMEM medium without glutamine nor branched chain amino acid (BCAA-)	Thermo Fisher Scientific	Cat# ME15212L1
DMEM medium without glutamine nor glucose (Glc-)	Thermo Fisher Scientific	Cat# A14430-01
Filtered foetal bovine serum	Hyclone	Cat# SH30070.02
Dialyzed foetal bovine serum	Hyclone	Cat# SH30079.02
Foetal bovine serum	BioSera	Cat# FB-1280
Antibiotic/antimycotic solution	Thermo Fisher Scientific	Cat# 15240062
Leucine	Sigma Aldrich	Cat# L8912
Isoleucine	Sigma Aldrich	Cat# I7403
Valine	Sigma Aldrich	Cat# V0513

Reagents and Tools table (continued)

Reagents or Tools	Source	Identifier
Sodium 3-hydroxybutyrate	Sigma Aldrich	Cat# 54965
Acetoacetate	Sigma Aldrich	Cat# A8509
L-Leucine (13C6)	Cambridge Isotope Laboratories	Cat# CLM-2262-H-PK
Sodium D-3-Hydroxybutyrate (13C4)	Cambridge Isotope Laboratories	Cat# CLM-3853-PK
L-glutamine (200 mM)	Thermo Fisher Scientific	Cat# 25030024
TransIT®-LT1	Mirus	Cat# MIR2300

Methods and Protocols

Spontaneous PDA models

Male PDA-bearing mice Pdx1-Cre; LSL-Kras^{G12D}; Ink4a/Arf^{fl/fl} (KIC), and control LSL-Kras^{G12D}; Ink4a/Arf^{fl/fl} (KI) littermates were obtained as previously described (Guillaumond *et al*, 2013). After sacrifice at 6 weeks ($n = 5$ KI mice and $n = 8$ KIC mice) or 9 weeks of age ($n = 3$ KI mice and $n = 3$ KIC mice), pieces of tumor or control pancreas were either fixed in 4% (wt/vol) formaldehyde, snap-frozen in cold isopentane for further analysis, or directly homogenized in 4 M guanidinium isothiocyanate lysis buffer for efficient pancreatic RNA extraction, according to previously published protocols (Guillaumond *et al*, 2013). All animal care and experimental procedures were performed in agreement with the Animal Ethics Committee of Marseille under reference (APAFIS#19183-2019021414576818). To study the impact of βOHB on tumors, 5-week-old KIC mice were daily injected for 3 weeks either with 100 mg/kg of βOHB or with an equivalent volume of 0.9% NaCl. After sacrifice, mice and tumors were weighed. Tumors, livers, and spleens were fixed in 4% (wt/vol) formaldehyde for histologic scoring and hematoxylin-phloxine-saffron (HPS) staining.

PDA xenograft models

Under isoflurane anesthesia [induction: 4% (vol/vol) and maintenance: 1.5% (vol/vol)], mice were injected subcutaneously with 0.2 mg/kg of buprenorphine (Vetergesic; Sogeval) and lidocaine (Xylovet; Ceva) was administered at 3.5 mg/kg by infiltration in the abdominal cavity. Five-week-old male HsdCpb:NMRI-Foxn1nu mice were orthotopically implanted with 1×10^6 of sg-CTRL PANC-1 cells ($n = 15$) or sg-HMGCL #2 clone ($n = 19$) or sg-HMGCL #3 clone ($n = 7$) PANC-1 cells. For βOHB treatment, mice were injected with 1×10^6 of sg-CTRL PANC-1 cells ($n = 4$) or sg-HMGCL #2,3 clones ($n = 20$). Seven days after engraftment, mice received twice a week 0.9% NaCl ($n = 4$ and $n = 10$ for sg-CTRL group and sg-HMGCL group, respectively) or 100 mg/kg of βOHB ($n = 10$ for sg-HMGCL group) for 2 months and sacrificed. At the time of sacrifice, tumors and livers were removed and weighed, and tumor length (L) and width (W) were determined with caliper. Tumor volume was determined with the following formula: $\pi/6 \times [(L + W)/2]^2$. Tumors and livers were fixed in 4% (wt/vol) formaldehyde. For collagen staining, Masson's trichrome coloration of formalin-fixed paraffin-embedded (FFPE) tumor sections was performed using an Artisan Link Special Staining System (Dako), according to manufacturer's instructions.

In ovo assay

Fertilized white Leghorn eggs were incubated at 37.5°C and 50% relative humidity for 9 days. At this time (E9), the chicken embryo

chorioallantoic membrane (CAM) was dropped by drilling a small hole through the eggshell into the air sac and a 1 cm² window was cut in the eggshell above the CAM. 3×10^6 sg-CTRL and sg-HMGCL #2 clone PANC-1 cells were inoculated onto the CAM of each egg ($n = 8$ eggs/group). At embryonic day 18 (E18), a 1 cm² portion of the lower CAM was collected to evaluate the number of metastatic cells. Genomic DNA was extracted from the lower CAM and analyzed by qPCR with specific primers for Alu sequences (Zijlstra *et al*, 2002). Data were analyzed with CFX Manager 3.1 software (Bio-Rad).

Assessment of βOHB injection or leucine-enriched diet on liver metastasis

As an induced metastatic model, KI mice were injected in two distinct liver lobes with 1×10^5 PK4A cells. Three days post-engraftment, mice were daily treated with 0.9% NaCl ($n = 8$) or 100 mg/kg of βOHB ($n = 8$) for 10 days. To evaluate the effect of leucine-enriched diet on liver metastasis, control amino acid defined diet (L-leucine 12 g/kg, TD110839, Envigo) and leucine-enriched diet (L-leucine 24 g/kg, TD110842 produced as isocaloric diet based on control diet TD110839, Envigo) were used. Mice were fed these diets one week before cell engraftment, for treatment of 18 days total. At the end of the experiments, livers were removed, washed with PBS 1×, and then fixed in 4% (wt/vol) formaldehyde. For each mouse, 1, 2, or 3 liver lobes with macroscopic metastasis were paraffin-embedded. 5 μm tissue sections were stained by HPS method. HPS-stained slides were scanned at 10× and 20× magnification. Liver metastasis characterization was performed by counting the number of metastasis per slide divided by the number of lobes present on the slide, and then classified into three different subtypes: small-, medium-, and large-size metastasis. In addition, anatomopathological status of metastasis was determined for each metastasis. Three different statuses were defined: undifferentiated, differentiated, and glandular metastasis.

Cell culture conditions

PK4A cell line was isolated from KIC murine PDA as previously described (Olivares *et al*, 2017), and used from passages 18–28. PANC-1 and MiaPaCa-2 cells were obtained from the American Type Culture Collection. Cells were maintained in 25 mM glucose, glutamine free Dulbecco's modified Eagle's medium (DMEM) without pyruvate, supplemented with 2 mM of L-glutamine, 10% (vol/vol) fetal bovine serum (FBS). Human PDA and liver metastasis-derived primary cell cultures were obtained as previously described (Nicolle *et al*, 2021). Briefly, PDA- and liver metastasis-PDX (patient-derived-xenograft) samples were split into several small pieces (1 mm³) and processed in a biosafety

chamber. After a fine mincing, they were treated with collagenase type V (C9263; Sigma-Aldrich, Inc., St. Louis, Missouri, USA) and trypsin/EDTA and suspended in DMEM supplemented with 1% w/w penicillin/streptomycin and 10% of FBS. After centrifugation, cells were re-suspended in Serum Free Ductal Media (SFDM) adapted from Schreiber *et al* (2004) and conserved at 37°C in a 5% CO₂ incubator. The three PDA patients from which the PDA- and liver metastasis-primary cell cultures are originated are part of the PaCaOmics cohort registered under the Paoli-Calmettes Institute clinical trial number 2011-A01439-32. For survival assays under leucine-deprived conditions, PK4A cells were cultured in 25 mM glucose, glutamine, and branched-chain amino acids (BCAAs) free Dulbecco's modified Eagle's medium DMEM without pyruvate, supplemented with 2 mM of L-glutamine, with 10% filtered FBS (SH30070, Hyclone), 1 mM of valine, isoleucine, and leucine (untreated medium), or with dialyzed FBS (SH30079, Hyclone), 1 mM of valine, isoleucine (Leu⁻ medium) with or without 10 mM of βOHB. For nutrient uptake experiments, glucose free-media (glc-) consists of glutamine-free DMEM without glucose nor pyruvate and supplemented with 2 mM of L-glutamine, 10% dialyzed FBS, and complete media consists of media used for cell maintenance, both with and without 1 mM of βOHB. Cells were cultured with 1% antibiotic/antimycotic solution at 37°C, 21% oxygen in a 5% CO₂ incubator and were mycoplasma free.

Murine PDA transcriptome analysis

All expression data from samples from 6-week (*n* = 5 control/healthy pancreas vs. 8 PDA) and 9-week (*n* = 3 control/healthy pancreas vs. *n* = 3 PDA), old mice were normalized with the Robust Multichip Average (RMA; Irizarry *et al*, 2003) from the package oligo available on Bioconductor (R 3.4.4 software). Gene Set Enrichment Analysis (GSEA) based on the Kyoto Encyclopedia of Genes and Genomes (KEGG) database was carried out with the R package fgSEA. The expression fold changes have been used as input of the function fgsea. Leading-edge genes correspond to the core genes that account for the gene set's enrichment signal (Subramanian *et al*, 2005). Hence, the leading-edge gene number is expressed as the percentage of deregulated leading-edge genes on total genes that compose each metabolic pathway (Appendix Table S1).

For differential BCAA and KB gene expression analysis, we only considered genes that are exclusively involved in BCAA catabolism and we added genes coding for BCAA and KB transporters to obtain a full representation of BCAA and KB metabolism in PDA. Genes differentially expressed between PDA and control pancreas from 6- or 9-week-old PKI and KI mice (Appendix Table S2) were determined by a *t*-test applied on the normalized RMA expression. The *P*-values were adjusted for multiple testing with the Benjamini-Hochberg method. Only genes with absolute fold change > 1.5 or > 2 and adjusted *P*-value < 0.05 are considered as significantly deregulated in 6- or 9-weeks PDA, respectively (Appendix Table S2) and are highlighted in volcano plots. For these illustrations, fold-changes and raw *P*-values are transformed into log₂ and -log₁₀ values, respectively. The dashed horizontal lines represent the selection cut-off based on the adjusted *P*-value cutoff threshold of 0.05. This cut-off does not match the same raw *P*-value (y-axis) for the two datasets since the calculated adjusted *P*-values depend on the input raw *P*-values.

KB gene expression in human PDA samples

We collected gene expression data of 728 pancreatic carcinomas and 76 metastatic samples (metastasis sites coming from liver (*n* = 35, 46%), peritoneal (*n* = 12, 16%), lymph node (*n* = 9, 12%), lung (*n* = 8, 11%), abdominal wall (*n* = 3, 4%), diaphragm (*n* = 3, 4%), colon (*n* = 2, 3%), duodenum (*n* = 2, 3%), and fat (*n* = 2, 3%)) from 15 public data sets from the National Center for Biotechnology Information (NCBI)/Genbank GEO, ArrayExpress, European Genome-phenome Archive (EGA), and TCGA databases (Appendix Table S4). Data analysis required pre-analytic processing and normalization as previously described (Birnbaum *et al*, 2017). KB gene expression levels were extracted from each data set and were standardized within each data set using the primary cancer population of the largest set as a reference to be comparable across data sets and to exclude bias from population heterogeneity. All steps were done in R using Bioconductor and associated packages.

Human samples

Freshly frozen tissue samples of PDA (*n* = 5) and corresponding healthy/adjacent pancreas (*n* = 5) located at distant site from the tumor were obtained from patients who underwent surgery. Histologic examination confirmed diagnosis of PDA and of healthy pancreases. Tumor staging was performed according to the International Union Against Cancer TNM system. All patients underwent surgery at the Department of Digestive Surgery, North Hospital, Marseille, France between 2009 and 2010. Before surgery, all patients had signed an informed consent form that had been approved by the local ethics committee (agreement reference of CRO2 tissue collection: DC-2013-1857; Marseille, France).

Protein extracts and western blots

Pancreatic ductal adenocarcinoma, healthy pancreas samples from PKI and KI mice and cell pellets were lysed in SDS 0.1%, 1% Triton X-100, Tris pH8 0.01 M and NaCl 0.14 M supplemented with 1 mM Phenylmethylsulfonyl fluoride, 100 μM orthovanadate, 40 mM β-glycerophosphate, 1 mM Sodium Fluoride, protease inhibitor cocktail (Sigma Aldrich), and sodium deoxycholate 1 or 10% for tissue or cells respectively, prior to centrifugation (14,000 rpm, 10 min, 4°C). Supernatants were collected, and protein concentration was evaluated using BioRad Protein assay. Whole cell protein extracts (75–100 μg/lane) were resolved by SDS/PAGE using a 10% (vol/vol) acrylamide gel and transferred onto 0.2 μm nitrocellulose membranes (Bio-Rad). After a blocking step (5% (wt/vol) non-fat milk in Tris-Buffered Saline (TBS)), primary antibody was incubated overnight (O/N) at 4°C (in 5% (wt/vol) non-fat milk in TBS 0.1% Tween 20). ECL protein detection (Millipore) was performed with a Fusion FX7 chemiluminescent imager and the quantification of the amounts of proteins of interest was determined by densitometry using Image J software (NIH) and normalized to ACTIN or to total loaded protein stained with Amido black or Ponceau Red.

Immuno-histochemistry

Formalin-fixed paraffin-embedded sections of mouse PDA (5 μm-thick) were deparaffinized in xylene and rehydrated through a series of graded ethanol concentrations. Antigen retrieval was performed in citrate buffer pH6 (Diapath)/ 0.05% Tween 20 or in target retrieval solution at pH 6 or 9 (Dako), before the quenching of endogenous peroxidase activity (3% (vol/vol) H₂O₂). Tissue

sections were then incubated with blocking solution prior to primary antibody. Immunoreactivity was visualized using the Vectastain ABC kit (PK-4001, Vector Laboratories) or with a biotinylated goat anti-rabbit antibody and peroxidase-conjugated streptavidin from Dako (France). Peroxidase activity was revealed using liquid DAB⁺ substrate chromogen system (Dako). Counter-staining in Mayer's Haematoxilin was followed by a bluing step in sodium bicarbonate buffer (0.1% in water) before final dehydration and mounting of the sections. Quantifications of staining were performed on seven pictures at 10 \times or 20 \times magnification using ImageJ software (NIH).

Establishment of sg-HMGCL cell lines

PANC-1 and MiaPaCa-2 cells were seeded on 6-well plates 24 h before being transfected with a pool of 3 HMGCL Crispr/Cas9 knock-out plasmids or with a Crispr/Cas9 control plasmid. Each plasmid codes for the Cas9 nuclease, a Green Fluorescent Protein (GFP), and a target-specific 20 nt guide RNA (gRNA). PANC-1 and MiaPaCa-2 cells were co-transfected with a Homology-Directed Repair (HDR) plasmid coding for a Red fluorescent protein (RFP) and containing a puromycin resistance gene. Forty-eight hour after transfection performed with Lipofectamine 3000, PANC-1-RFP cells were cloned by cell sorting using fluorescence-activated cell sorting (FACS) (AriallII, BD Biosciences) and only PANC-1 clones depleted in HMGCL were selected and maintained upon puromycin treatment. For sg-HMGCL MiaPaCa-2 cells, clones were isolated using limiting dilution and maintained upon puromycin treatment.

Establishment of ALCAM⁺ and SQLE⁺ PANC-1 cell lines

sg-HMGCL PANC-1 cells were seeded on 6-well plates with 2 \times 10⁵ cells per well 24 h before transfection. Using TransIT[®]-LT1, cells were transfected with either an empty pcDNA3.1(+)-N-DYK plasmid, or a pcDNA3.1(+)-N-DYK plasmid containing SQLE or ALCAM cDNA. All plasmids contain both a flag on the N-terminus and a neomycin resistance gene. Forty-eight hour post-transfection, stable transfected cells were selected and maintained upon neomycin treatment.

Survival assays

7 \times 10⁴ PK4A cells were plated in 48-well plates using experimental media as described above in Methods and Protocols. Media were changed at day 3. Percentage of confluence was assessed every day for 5 days using IncuCyte[™] S3 Live-Cell analysis system (Sartorius).

Proliferation assays

sg-CTRL or sg-HMGCL PANC-1 cells or MiaPaCa-2 cells (3 \times 10⁴) were plated in 48-well plates, in triplicates, using media for their maintenance as described above in Methods and Protocols. After the indicated times, triplicates were pooled, and viability was assessed via Trypan blue exclusion using a cell viability analyzer (Vi-cell XR, Beckman Coulter).

Clonogenic assays

1,000 sg-CTRL or sg-HMGCL PANC-1 and MiaPaCa-2 cells were seeded in a 6-well plate and cultured in the same medium as for their maintenance. Fifteen days later, colonies were fixed in 10% (wt/vol) formalin and stained with 0.5% Crystal violet. Pictures were captured using an Evos microscope (Thermo Fisher Scientific)

at 4 \times magnification, and areas of stained colonies were quantified by ImageJ software (NIH). Representative pictures for illustration were obtained using a camera.

Migratory assays

Three 10⁴ sg-CTRL and sg-HMGCL PANC-1 cells were seeded in the same medium as for their maintenance without FBS in a 24-well insert, pre-coated with 1% of gelatin and 0.1% of fibronectin, and placed in a 24-well plate containing the same media with 10% FBS. Four hour after seeding, inserts were fixed in 10% (wt/vol) methanol, stained with Coomassie bleu. Seven pictures of each well were captured using an Evos microscope at 4 \times magnification and quantified by ImageJ software.

Wound-healing assays

7.5 \times 10⁵ sg-CTRL and sg-HMGCL PANC-1 cells and MiaPaCa-2 cells were seeded in 6-well plates in the same medium as for their maintenance. To inhibit proliferation, cells were rendered quiescent using mitomycin C (0.5 μ g/ml) 2 h before scratch. After scratch, wells were washed with PBS 1 \times , and fresh medium containing mitomycin C (0.5 μ g/ml) was added. Images were captured at 0 h and 72 h after scratch, at 2 \times magnification. Scratched area recovered by cells was measured using ImageJ software and expressed as percentage of measured initial scratched area at day 0.

Invasion assays

4.5 \times 10⁴ sg-CTRL and sg-HMGCL PANC-1 cells were seeded in the same medium as for their maintenance without FBS into 24-well invasion chambers already pre-coated with matrigel and placed in a 24-well plate containing the same medium as for their maintenance. Twenty-four hour after invasion, inserts were fixed in 10% (wt/vol) methanol, stained with Coomassie bleu. Images were obtained using an Evos microscope and the number of invasive cells was quantified by ImageJ software. For spheroid invasion assays, 1,500 sg-CTRL and sg-HMGCL PANC-1 cells were seeded in the same medium as for their maintenance in 96-well ultra-low attachment plate (Corning). After 3 days in culture, 100 μ l of medium was replaced by 100 μ l of cold matrigel (Corning). Plates were centrifuged 5 min at 4°C to allow the dilution of matrigel in medium and placed for 1 h in a 37°C incubator for matrigel polymerization before adding 100 μ l of medium. Pictures were captured at day 10 or 15 at 2 \times , 4 \times , 10 \times , or 20 \times magnifications to observe invasive cells.

Spheroid/organoid assays

1,500 cells were seeded in 96-well ultra-low attachment plate (Corning) and cultured as spheroids in the same medium as for their maintenance. For PK4a spheroids, media containing 1 or 10 mM of β OHb, or not (untreated), were replenished at day 3, 7 and 10. Spheroids area was assessed every day for 12 days using IncuCyte[™] S3 Live-Cell analysis system (Sartorius). For sg-CTRL and sg-HMGCL PANC-1 spheroids, media was replenished twice a week. Pictures of PANC-1 spheroids were captured using Evos microscope at 2, 4, or 10 \times magnification. After 15 days, PANC-1 spheroids were dissociated using trypsin, and cells were counted via Trypan blue exclusion. For mouse and human PDA- or liver metastasis-derived organoids, we cultured 5 \times 10⁴ cells in Pancreatic Organoid Feeding Media (POFM) medium after seeding in 48-well plate pre-coated with Matrigel as previously described (Hoare *et al*, 2021). After

2 days, once the organoids were formed, media were replaced by the same medium as for their maintenance alone or with 1 or 10 mM of β OHB. Pictures of organoids were captured using Evos microscope at 4 \times magnification.

Quantification of cell fluorescent dye

To analyze proliferation of cells, CellTrace™ Carboxyfluorescein Succinimidyl Ester (CFSE) Cell proliferation Kit was used according to the manufacturer's protocol. Briefly, before seeding, sg-CTRL and sg-HMGCL PANC-1 cells were incubated for 20 min with 5 μ M of CFSE in a 37°C incubator, then washed twice with PBS 1 \times containing 2% FBS. 3.5×10^5 cells were seeded in 2 ml of medium in 6-well plates and maintained for 3 days. For spheroid assays, 1,500 cells were seeded in 200 μ l of medium in a 96-well ultra-low attachment plate (corning) and maintained for 7 days. At the indicated times, cells were detached and washed with PBS 1 \times . Mean fluorescence intensity (MFI) of each cell line was measured with the MACSQuant-VYB cytometer and then reported as the percentage of MFI as indicated in figure legends, using FlowJo software, in order to evaluate the proliferation index.

Tracing experiments

For *in vitro* tracing of leucine or β OHB, 7.5×10^4 of PK4A, sg-CTRL or sg-HMGCL PANC-1 cells were plated in triplicate in 6-well plates in medium used for their maintenance. The following day, cells were washed with PBS 1 \times and refreshed with DMEM without glucose, nor pyruvate, nor glutamine, and supplemented or not with 5 mM or 25 mM of glucose and with 2 mM L-glutamine, 10% dialyzed FBS, and 0.8 mM U-¹³C-Leucine or 1 mM U-¹³C- β OHb for 24 h at 37°C. Then, cells were harvested, extracted, and analyzed as described below. For *ex vivo* tracing, tumors were collected from KIC mice at 6- or 9-weeks of age. After collection, thin slices (around 500 μ m) were performed from a piece of tumor and then washed twice with PBS 1 \times and cultured in DMEM with 10% dialyzed FBS without glucose, nor pyruvate, nor glutamine supplemented with 2 mM L-glutamine and 25 mM U-¹³C-Glucose, or without glutamine and supplemented with 2 mM U-¹³C-Glutamine or supplemented with 2 mM L-glutamine, 1 mM U-¹³C- β OHb, or 0.2 mM U-¹³C-Acetate, for 24 h. After that, tumor slices were harvested, washed, grounded to powder, and metabolites were extracted and analyzed as described below. A piece of the initial tumor was fixed in 4% (wt/vol) formaldehyde for further histological analysis.

Extraction of metabolites

At the conclusion of the tracing experiments, *ex vivo* tumors, PK4A, sg-CTRL, or sg-HMGCL PANC-1 cells were rinsed once in blood bank saline, and metabolites were extracted with a methanol:chloroform:water (5:5:3) mix containing norvaline as an internal standard, as previously described (Olivares *et al.*, 2017). After vortexing and centrifugation, the aqueous phase containing polar metabolites was removed, dried under nitrogen gas, and stored at -80°C for subsequent derivatization. Samples were then run on the Gas Chromatography/Mass Spectrometry (GC/MS) as described in the following section.

GC/MS analyses

Dried polar metabolites were dissolved in 20 μ l of pyridine containing 2% of methoxamine hydrochloride (Thermo Fisher

Scientific) and held at 37°C for 1 h. After dissolution and reaction, tert-butyl-di-methyl-silyl derivatization was initiated by adding 25 μ l N-methyl-N-(tert-butyl-di-methyl-silyl) trifluoroacetamide + 1% tert-butyl-dimethyl-chlorosilane (Sigma Aldrich) and by incubating at 37°C for 30 min. GC/MS analysis was performed using an Agilent 7890 GC equipped with a 30 m DB-35MS capillary column connected to an Agilent 5975B MS operating under electron impact ionization at 70 eV. One microliter of sample was injected in splitless mode at 270°C, using helium as the carrier gas at a flow rate of 1.2 ml/min. For measurement of polar metabolites, the GC oven temperature was held at 100°C for 1 min, increased to 105°C at 2.5°C/min and held at 105°C for 2 min, increased to 250°C at 3.5°C/min, and increased to 320°C at 20°C/min. The MS source and quadrupole were held at 230°C and 150°C, respectively, and the detector was run in scanning mode, recording ion abundance in the range of 100–605 m/z. MIDs were determined by integrating the appropriate ion fragments.

Nutrient uptake analysis

Glucose and glutamine consumption were assessed using the YSI 2950 BioAnalyser (System-C-Industry). Briefly, triplicates of sg-CTRL or sg-HMGCL PANC-1 cells were seeded (3×10^4 cells) in 48-well plates in experimental media as described above. After 72 h, supernatants were collected and metabolite concentrations of glutamine and glucose were measured. Viable cells numbers were evaluated through Trypan blue exclusion using a cell viability analyzer (Vi-cell XR, Beckman Coulter) and used for normalization. For every metabolite measurement, fresh maintenance or glc free media were used as starting point for baseline concentrations.

Mass spectrometry proteomic analysis

Extraction of proteins from sg-CTRL and sg-HMGCL (#2 and #3) PANC-1 spheroids was performed as previously described. 15 μ g of each protein sample of each cell line was loaded on a NuPAGE gel 4–12% (Life Technologies) and run as a single band for a 6 min electrophoresis at 80V in MOPS buffer (Thermo Fisher Scientific). Gels were incubated with Imperial Protein Stain (Thermo Fisher Scientific) and after extensive washes, stacked protein bands were cut and submitted to classical in gel protein digestion (reduction, iodoacetamide alkylation, and trypsin digestion). Extracted peptides were concentrated under speed vacuum and solubilized in 2% acetonitrile, 0.05% Trifluoroacetic acid. For mass spectrometry acquisition, 20% of each sample was injected in triplicates on a liquid nanochromatography Ultimate 3000RSCL system (Thermo Fisher Scientific) online in front of an Orbitrap Fusion Lumos Tribrid mass spectrometer (Thermo Fisher Scientific). Peptides were first concentrated and purified on a pre-column from Dionex (C18 PepMap100, 2 cm \times 100 μ m I.D, 100 Å pore size, 5 μ m particle size) in solvent A (0.1% formic acid in 2% acetonitrile). In the second step, peptides were separated on a reverse phase LC EASY-Spray C18 column from Dionex (PepMap RSLC C18, 50 cm \times 75 μ m I.D, 100 Å pore size, 2 μ m particle size) at 300 nL/min flow rate and 40°C. After column equilibration using 4% of solvent B (20% water–80% acetonitrile–0.1% formic acid), peptides were eluted from the analytical column by a two-step linear gradient (4–22% acetonitrile/H₂O; 0.1% formic acid for 220 min and 22–32% acetonitrile/H₂O; 0.1% formic acid for 20 min). For peptide ionization in the EASY-Spray nanosource, spray voltage was set at

2.2 kV and the capillary temperature at 275°C. The mass spectrometer was used in data-dependent mode to switch consistently between MS and MS/MS. Time between Masters Scans was set to 3 s. MS spectra were acquired with the Orbitrap in the range of m/z 400–1,600 at a FWHM resolution of 120,000 measured at 200 m/z . AGC target was set at 4.0e5 with a 50 ms Maximum Injection Time. The more abundant precursor ions were selected, and collision-induced dissociation fragmentation at 35% was performed and analyzed in the ion trap using the “Inject Ions for All Available Parallelizable time” option with a maximum injection time of 300 ms and an AGC target of 4000. Charge state screening was enabled to include precursors with 2 and 7 charge states. Dynamic exclusion was enabled with a repeat count of 1 and a duration of 60 s. These chromatographic conditions were previously optimized with a protein pool from all the samples.

Quantitative proteomics processing

For data processing, we used the free suite MaxQuant version 15.3.8 (Cox *et al*, 2011). The relative intensities based on label-free quantification (LFQ) were calculated using the MaxLFQ algorithm (Cox *et al*, 2014). The 27 LC-MS raw acquisitions were processed by the Andromeda search engine integrated into MaxQuant (Cox *et al*, 2011). The identification of the precursor ions present in the mass spectra was performed by comparison with the protein database of Human extracted from Uniprot on the 31st of May 2017 and containing 20,200 entries. This database was supplemented with a set of 245 proteins that are commonly found as contaminants. The following parameters were used for this search: (i) trypsin cleavage authorization before prolines; (ii) authorization of two failed cleavages; (iii) fixed modification of cysteines by carbamidomethylation (+57.02146 Da) and variable modification of methionines by oxidation (+15.99491) and N-terminal proteins by acetylation (+42.0116); (iv) authorization of five modifications per peptide; and (v) minimum peptides length of seven amino acids and a maximum mass of 4,600 Da. Spectra alignment was performed in two dimensions; the elution time of the precursor ions (min) and the mass range. The “Match between runs” option has been enabled to allow the transfer of identifications between LC-MS/MS based on the mass and the retention time using the default settings. The false positive rate on identification was set at 1%. The statistical analysis was carried out with the Perseus program (version 1.6.0.7) of the MaxQuant environment. The normalized intensity LFQ was transformed by a base logarithm 2 to obtain a normal distribution. Differential proteins were evidenced by the application of a multiple ANOVA *t*-test or a Student *t*-test performed by controlling the false positive rate at 1% using 250 permutations. Proteins differently expressed between samples were analyzed based on the \log_2 difference of the LFQ intensity and \log_{10} of the associated *q* value. For visualization of proteomic data sets, volcano plots were created using a cutoff of *q*-value < 0.05 and a cutoff of difference of LFQ intensity of < -2.3 or > 2.3 between compared groups. The differential proteomics analysis was carried out on identified proteins after removal of proteins only identified with a modified peptide, peptides shared with other proteins, proteins from contaminant database and proteins which are only represented in two replicates of six of the same condition. Common proteins with deregulated expression levels in sg-HMGCL #2 and #3 compared to sg-CTRL PANC-1 cells were then further analyzed.

ALCAM staining

4×10^5 sg-CTRL or sg-HMGCL PANC-1 cells were detached from plate with accutase, transferred to a 96 round bottom well plate, and were incubated with anti-ALCAM antibody diluted in PBS 1× containing 2% FBS and 5% EDTA during 30 min at 37°C. Then, cells were washed three times before being incubated with secondary antibody at 37°C for 30 min. MFI of 10,000 cells for each cell line was measured with the MACSQuant –VYB cytometer and analyzed with FlowJo software, in order to evaluate ALCAM quantity.

Reverse transcription

5×10^5 cells were plated in 6 cm dish at day 0 in maintenance medium. The day after, cells were washed twice with PBS 1× and RNA was extracted by Trizol reagent. 5 µg of total RNA were used to synthesize cDNA with the PrimeScript RT reagent kit (Promega) and provided oligo-dT primers, according to the manufacturer’s instructions.

Quantitative real-time polymerase chain reaction (qPCR)

Quantitative PCR reactions were performed with *EPHA2*, *FLNB*, and *PLAU* specific primers and the GoTaq qPCR master mix kit (Promega) using the Mx3005P Stratagene system. Differential expression of transcripts of interest was normalized with the respective *36B4* housekeeping transcript expression.

Statistical analysis

One-tailed unpaired Student’s *t*-test was used for comparing means of two experimental groups in the case of one independent factor; for *in vitro* experiments comparing sg-CTRL vs. sg-HMGCL samples, we compared the overall changes between the two groups (*i.e.* mean of all sg-HMGCL samples vs. sg-CTRL samples). For all *in vivo* experiments, we used a Mann-Whitney non-parametric test to compare two experimental groups when data do not follow a normal distribution. One way or two-way ANOVA, followed by the appropriated multiple comparison test, was used when comparing more than two experimental groups. In all figures, data are presented as a mean ± standard error of the mean (SEM) and exact *n* values used to calculate the statistics are indicated. All statistical analyses were performed using GraphPad Prism 5. *P*-values < 0.05 were considered statistically significant.

Data availability

For expression data from samples from 6-week (*n* = 5 control pancreas vs 8 PDA) and 9-week (*n* = 3 control pancreas vs *n* = 3 PDA) old mice, the DNA microarray raw data have been deposited in Gene Expression Omnibus under: GSE127891 (<https://www.ncbi.nlm.nih.gov/geo/query/acc.cgi?acc=GSE127891>) (6-week RMA data) and GSE61412 (<https://www.ncbi.nlm.nih.gov/geo/query/acc.cgi?acc=GSE61412>) (9-week RMA data).

Expanded View for this article is available online.

Acknowledgements

We thank the cell culture platform (PCC, TPR2, CRCM, Marseille, France), the mice colony facility (PSEA, TPR2, CRCM, Marseille, France), the bioinformatic platform (Cibi, CRCM, Marseille, France), proteomics platform (CRCM,

Marseille, France) for technical assistance. V.G. was supported by the “Ligue contre le cancer” and the “Association pour la Recherche sur le Cancer, ARC.” T.G. was supported by the National Institute of Cancer (INCaPLBIO15-217). E.J.P. was supported by the Foundation for Medical Research (FRM), C.D. was supported by the National Institute of Cancer (INCa Pair Pancreas 2018-082), E.M. was supported by the French Ministry for Research and Education (MENRT). E.C.L. is a Damon Runyon Fellow supported by the Damon Runyon Cancer Research Foundation (DRG-2299-17). J.R.M. was supported by F30CA183474 from the NCI. MGVH acknowledges support from the Lustgarten Foundation, the MIT Center for Precision Cancer Medicine, SU2C, the Ludwig Center at MIT, the NCI (R35-CA242379, R01CA168653, R01CA201276, P30CA1405141), the Emerald Foundation, and is a faculty scholar award from the Howard Hughes Medical Institute. SV acknowledges supports from the National Institute of Cancer (INCa PLBIO15-217, INCa Pair Pancreas 2018-082), the Plan Cancer 2009–2013 (C13056AS), the Foundation for Medical Research (FRM SPF2018096968), the association for cancer research (ARC, PJA-20181208127), and the Cancéropôle PACA (2019-00100).

Author contributions

Victoire Gouirand: Conceptualization; Data curation; Validation; Methodology; Writing—original draft; Writing—review and editing. **Tristan Gicquel:** Conceptualization; Data curation; Methodology. **Evan C Lien:** Conceptualization; Data curation; Formal analysis; Writing—original draft; Writing—review and editing. **Emilie Jaune-Pons:** Data curation; Methodology. **Quentin Da Costa:** Conceptualization; Methodology; Writing—original draft. **Pascal Finetti:** Data curation; Writing—original draft. **Elodie Metay:** Data curation; Methodology. **Camille Duluc:** Methodology. **Jared R Mayers:** Methodology. **Stephane Audebert:** Methodology; Writing—original draft. **Luc Camoin:** Conceptualization; Methodology. **Laurence Borge:** Methodology. **Marion Rubis:** Methodology. **Julie Leca:** Resources; Methodology. **Jeremy Nigri:** Methodology. **François Bertucci:** Conceptualization; Methodology; Writing—original draft. **Nelson Dusetti:** Resources; Methodology. **Juan Lucio Iovanna:** Resources; Methodology. **Richard Tomasini:** Conceptualization; Resources; Methodology. **Ghislain Bidaut:** Conceptualization; Data curation; Methodology. **Fabienne Guillaumond:** Conceptualization; Methodology; Writing—review and editing. **Matthew G Vander Heiden:** Conceptualization; Funding acquisition; Methodology; Writing—original draft; Writing—review and editing. **Sophie Vasseur:** Conceptualization; Resources; Data curation; Formal analysis; Supervision; Funding acquisition; Validation; Investigation; Methodology; Writing—original draft; Project administration; Writing—review and editing.

In addition to the CRediT author contributions listed above, the contributions in detail are

VG, TG, ECL, EJ-P, CD, and EM performed the experiments. VG, ECL, JRM, and MGVH performed and assisted tracing experiments and GC/MS analysis. QDC and GB analyzed the mouse transcriptomic datasets. PF and FB provided and analyzed human transcriptomic datasets. LC and SA performed proteomics and data analysis. LB and JN assisted and provided advice for cell culture. MR assisted immunochemistry experiments. ND and JLI provided human PDA and liver metastatic derived primary cells. RT and JL provided protein extracts from human samples. SV, VG, MGVH, FG, and RT conceptualized the study. FG and RT provided advice regarding experiments and writing of the manuscript. SV directed the study. SV, MGVH, VG, ECL, PF, QDC, and FG wrote the manuscript. Funding acquisition, SV, MGVH, and FG.

Disclosure and competing interests statement

MGVH discloses that he is on the scientific advisory board of Agios Pharmaceuticals, iTeos Therapeutics, Drioia Ventures, Sage Therapeutics, and Auron Therapeutics. Other authors declare that they have no conflict of interest.

References

- Aguirre AJ, Bardeesy N, Sinha M, Lopez L, Tuveson DA, Horner J, Redston MS, DePinho RA (2003) Activated Kras and Ink4a/Arf deficiency cooperate to produce metastatic pancreatic ductal adenocarcinoma. *Genes Dev* 17: 3112–3126
- Badgley MA, Kremer DM, Maurer HC, DelGiorno KE, Lee H-J, Purohit V, Sagalovskiy IR, Ma A, Kapilian J, Firl CEM et al (2020) Cysteine depletion induces pancreatic tumor ferroptosis in mice. *Science* 368: 85–89
- Bagci T, Wu JK, Pfannl R, Ilag LL, Jay DG (2009) Autocrine semaphorin 3A signaling promotes glioblastoma dispersal. *Oncogene* 28: 3537–3550
- Biancur DE, Kapner KS, Yamamoto K, Banh RS, Neggers JE, Sohn ASW, Wu W, Manguso RT, Brown A, Root DE et al (2021) Functional genomics identifies metabolic vulnerabilities in pancreatic cancer. *Cell Metab* 33: 199–210
- Biancur DE, Paulo JA, Małachowska B, Quiles Del Rey M, Sousa CM, Wang X, Sohn ASW, Chu GC, Gygi SP, Harper JW et al (2017) Compensatory metabolic networks in pancreatic cancers upon perturbation of glutamine metabolism. *Nat Commun* 8: 15965
- Birnbaum DJ, Finetti P, Lopresti A, Gilabert M, Poizat F, Raoul J-L, Delpere J-R, Moutardier V, Birnbaum D, Mamessier E et al (2017) A 25-gene classifier predicts overall survival in resectable pancreatic cancer. *BMC Med* 15: 170
- Chakrabarti G, Moore ZR, Luo X, Ilcheva M, Ali A, Padanad M, Zhou Y, Xie Y, Burma S, Scaglioni PP et al (2015) Targeting glutamine metabolism sensitizes pancreatic cancer to PARP-driven metabolic catastrophe induced by ss-lapachone. *Cancer Metab* 3: 12
- Commissio C, Davidson SM, Soydaner-Azeloglu RG, Parker SJ, Kamphorst JJ, Hackett S, Grabocka E, Nofal M, Drebin JA, Thompson CB et al (2013) Macropinocytosis of protein is an amino acid supply route in Ras-transformed cells. *Nature* 497: 633–637
- Cox J, Hein MY, Luber CA, Paron I, Nagaraj N, Mann M (2014) Accurate proteome-wide label-free quantification by delayed normalization and maximal peptide ratio extraction, termed MaxLFQ. *Mol Cell Proteomics* 13: 2513–2526
- Cox J, Neuhauser N, Michalski A, Scheltema RA, Olsen JV, Mann M (2011) Andromeda: a peptide search engine integrated into the MaxQuant environment. *J Proteome Res* 10: 1794–1805
- Daher B, Parks SK, Durivault J, Cormerais Y, Baidarjad H, Tambutte E, Pouyssegur J, Vucetic M (2019) Genetic ablation of the cystine transporter xCT in PDAC cells inhibits mTORC1, growth, survival, and tumor formation via nutrient and oxidative stresses. *Cancer Res* 79: 3877–3890
- Davidson SM, Jonas O, Keibler MA, Hou HW, Luengo A, Mayers JR, Wyckoff J, Del Rosario AM, Whitman M, Chin CR et al (2017) Direct evidence for cancer-cell-autonomous extracellular protein catabolism in pancreatic tumors. *Nat Med* 23: 235–241
- De Feyter HM, Behar KL, Rao JU, Madden-Hennessey K, Ip KL, Hyder F, Drewes LR, Geschwind JF, de Graaf RA, Rothman DL (2016) A ketogenic diet increases transport and oxidation of ketone bodies in RG2 and 9L gliomas without affecting tumor growth. *Neuro-oncology* 18: 1079–1087
- Devís L, Moiola CP, Masia N, Martínez-García E, Santacana M, Stirbat TV, Brochard-Wyart F, García Á, Alameda F, Cabrera S et al (2017) Activated leukocyte cell adhesion molecule (ALCAM) is a marker of recurrence and promotes cell migration, invasion, and metastasis in early-stage endometrioid endometrial cancer. *J Pathol* 241: 475–487
- Dumartin L, Quemener C, Laklai H, Herbert J, Bicknell R, Bousquet C, Pyronnet S, Castronovo V, Schilling MK, Bikfalvi A et al (2010) Netrin-1 mediates early events in pancreatic adenocarcinoma progression, acting on tumor and endothelial cells. *Gastroenterology* 138: 1595–1606

- Forlay J, Partensky C, Bray F (2016) More deaths from pancreatic cancer than breast cancer in the EU by 2017. *Acta Oncol* 55: 1158–1160
- Gouirand V, Guillaumond F, Vasseur S (2018) Influence of the tumor microenvironment on cancer cells metabolic reprogramming. *Front Oncol* 8: 117
- Gouirand V, Vasseur S (2018) Fountain of youth of pancreatic cancer cells: the extracellular matrix. *Cell Death Discov* 4: 1
- Grabacka MM, Wilk A, Antonczyk A, Banks P, Walczak-Tytko E, Dean M, Pierzchalska M, Reiss K (2016) Fenofibrate induces ketone body production in melanoma and glioblastoma cells. *Front Endocrinol* 7: 5
- Grünert SC, Schlatter SM, Schmitt RN, Gemperle-Britschgi C, Mrázová L, Balci MC, Bischof F, Çoker M, Das AM, Demirkol M et al (2017) 3-Hydroxy-3-methylglutaryl-coenzyme A lyase deficiency: clinical presentation and outcome in a series of 37 patients. *Mol Genet Metab* 121: 206–215
- Guillaumond F, Bidaut G, Ouaissi M, Servais S, Gouirand Vi, Olivares O, Lac S, Borge L, Roques J, Gayet O et al (2015) Cholesterol uptake disruption, in association with chemotherapy, is a promising combined metabolic therapy for pancreatic adenocarcinoma. *Proc Natl Acad Sci* 112: 2473–2478
- Guillaumond F, Leca J, Olivares O, Lavaut M-N, Vidal N, Berthezène P, Dusetti NJ, Loncle C, Calvo E, Turrini O et al (2013) Strengthened glycolysis under hypoxia supports tumor symbiosis and hexosamine biosynthesis in pancreatic adenocarcinoma. *Proc Natl Acad Sci USA* 110: 3919–3924
- Hagedorn M, Javerzat S, Gilges D, Meyre A, de Lafarge B, Eichmann A, Bikfalvi A (2005) Accessing key steps of human tumor progression in vivo by using an avian embryo model. *Proc Natl Acad Sci USA* 102: 1643–1648
- Hoare O, Fraunhoffer N, Elkaoutari A, Gayet O, Bigonnet M, Roques J, Nicolle R, McGuckin C, Forraz N, Sohier E et al (2021) Exploring the complementarity of pancreatic ductal adenocarcinoma preclinical models. *Cancers* 13: 2473
- Honkala AT, Tailor D, Malhotra SV (2019) Guanylate-binding protein 1: an emerging target in inflammation and cancer. *Front Immunol* 10: 3139
- Hopkins BD, Pauli C, Du X, Wang DG, Li X, Wu D, Amadiume SC, Goncalves MD, Hodakoski C, Lundquist MR et al (2018) Suppression of insulin feedback enhances the efficacy of PI3K inhibitors. *Nature* 560: 499–503
- Huang CK, Chang PH, Kuo WH, Chen CL, Jeng YM, Chang KJ, Shew JY, Hu CM, Lee WH (2017) Adipocytes promote malignant growth of breast tumours with monocarboxylate transporter 2 expression via beta-hydroxybutyrate. *Nat Commun* 8: 14706
- Huang DE, Li T, Wang L, Zhang L, Yan R, Li K, Xing S, Wu G, Hu L, Jia W et al (2016) Hepatocellular carcinoma redirects to ketolysis for progression under nutrition deprivation stress. *Cell Res* 26: 1112–1130
- Iriarri RA, Hobbs B, Collin F, Beazer-Barclay YD, Antonellis KJ, Scherf U, Speed TP (2003) Exploration, normalization, and summaries of high density oligonucleotide array probe level data. *Biostatistics* 4: 249–264
- Kamil M, Shinsato Y, Higa N, Hirano T, Idogawa M, Takajo T, Minami K, Shimokawa M, Yamamoto M, Kawahara K et al (2019) High filamin-C expression predicts enhanced invasiveness and poor outcome in glioblastoma multiforme. *Br J Cancer* 120: 819–826
- Kamphorst JJ, Nofal M, Commissio C, Hackett SR, Lu W, Grabocka E, Vander Heiden MG, Miller G, Drebin JA, Bar-Sagi D et al (2015) Human pancreatic cancer tumors are nutrient poor and tumor cells actively scavenge extracellular protein. *Cancer Res* 75: 544–553
- Kang H-B, Fan J, Lin R, Elf S, Ji Q, Zhao L, Jin L, Seo J, Shan C, Arbiser J et al (2015) Metabolic rewiring by oncogenic BRAF V600E links ketogenesis pathway to BRAF-MEK1 signaling. *Mol Cell* 59: 345–358
- Kessler SK, Neal EG, Camfield CS, Kossoff EH (2011) Dietary therapies for epilepsy: future research. *Epilepsy Behav* 22: 17–22
- Kim NI, Park MH, Kweon SS, Cho N, Lee JS (2021) Squalene epoxidase expression is associated with breast tumor progression and with a poor prognosis in breast cancer. *Oncol Lett* 21: 259
- Leca J, Martinez S, Lac S, Nigri J, Secq V, Rubis M, Bressy C, Sergé A, Lavaut M-N, Dusetti N et al (2016) Cancer-associated fibroblast-derived annexin A6⁺ extracellular vesicles support pancreatic cancer aggressiveness. *J Clin Invest* 126: 4140–4156
- Lee CL, Huang CJ, Yang SH, Chang CC, Huang CC, Chien CC, Yang RN (2016) Discovery of genes from feces correlated with colorectal cancer progression. *Oncol Lett* 12: 3378–3384
- Li X, Chen Q, Yin D, Shi S, Yu L, Zhou S, Chen E, Zhou Z, Shi Y, Fan J et al (2017) Novel role of semaphorin 3A in the growth and progression of hepatocellular carcinoma. *Oncol Rep* 37: 3313–3320
- Li Y, Zhang X, Ma A, Kang Y (2021) Rational application of beta-hydroxybutyrate attenuates ischemic stroke by suppressing oxidative stress and mitochondrial-dependent apoptosis via activation of the Erk/CREB/eNOS pathway. *ACS Chem Neurosci* 12: 1219–1227
- Lien EC, Westermark AM, Zhang Y, Yuan C, Li Z, Lau AN, Sapp KM, Wolpin BM, Vander Heiden MG (2021) Low glycaemic diets alter lipid metabolism to influence tumour growth. *Nature* 599: 302–307
- Liu KA, Lashinger LM, Rasmussen AJ, Hursting SD (2014) Leucine supplementation differentially enhances pancreatic cancer growth in lean and overweight mice. *Cancer Metab* 2: 6
- Luo W, Qin L, Li BO, Liao Z, Liang J, Xiao X, Xiao X, Mo Y, Huang G, Zhang Z et al (2017) Inactivation of HMGCL promotes proliferation and metastasis of nasopharyngeal carcinoma by suppressing oxidative stress. *Sci Rep* 7: 11954
- Mahoney CE, Pirman D, Chubukov V, Sleger T, Hayes S, Fan ZP, Allen EL, Chen Y, Huang L, Liu M et al (2019) A chemical biology screen identifies a vulnerability of neuroendocrine cancer cells to SQLE inhibition. *Nat Commun* 10: 96
- Makohon-Moore AP, Zhang M, Reiter JG, Bozic I, Allen B, Kundu D, Chatterjee K, Wong F, Jiao Y, Kohutek ZA et al (2017) Limited heterogeneity of known driver gene mutations among the metastases of individual patients with pancreatic cancer. *Nat Genet* 49: 358–366
- Martin PM, Gopal E, Ananth S, Zhuang L, Itagaki S, Prasad BM, Smith SB, Prasad PD, Ganapathy V (2006) Identity of SMCT1 (SLC5A8) as a neuron-specific Na⁺-coupled transporter for active uptake of L-lactate and ketone bodies in the brain. *J Neurochem* 98: 279–288
- Martinez-Outschoorn UE, Lin Z, Whitaker-Menezes D, Howell A, Lisanti MP, Sotgia F (2012) Ketone bodies and two-compartment tumor metabolism: stromal ketone production fuels mitochondrial biogenesis in epithelial cancer cells. *Cell Cycle* 11: 3956–3963
- Mayers JR, Torrence ME, Danai LV, Papagiannakopoulos T, Davidson SM, Bauer MR, Lau AN, Ji BW, Dixit PD, Hosios AM et al (2016) Tissue of origin dictates branched-chain amino acid metabolism in mutant Kras-driven cancers. *Science* 353: 1161–1165
- Mayers JR, Wu C, Clish CB, Kraft P, Torrence ME, Fiske BP, Yuan C, Bao Y, Townsend MK, Tworoger SS et al (2014) Elevation of circulating branched-chain amino acids is an early event in human pancreatic adenocarcinoma development. *Nat Med* 20: 1193–1198
- Mikaelian I, Malek M, Gadet R, Viallet J, Garcia A, Girard-Gagnepain A, Hesling C, Gillet G, Gonzalo P, Rimokh R et al (2013) Genetic and pharmacologic inhibition of mTORC1 promotes EMT by a TGF-beta-independent mechanism. *Cancer Res* 73: 6621–6631
- Mizrahi JD, Surana R, Valle JW, Shroff RT (2020) Pancreatic cancer. *Lancet* 395: 2008–2020

- Ni T, Wang H, Zhan D, Tao L, Lv M, Wang W, Chu Z, Zhou Z, Sunagawa M, Liu Y (2021) CD133+/CD166+ human gastric adenocarcinoma cells present the properties of neoplastic stem cells and emerge more malignant features. *Life Sci* 269: 119021
- Nicolle R, Gayet O, Duconseil P, Vanbrugghe C, Roques J, Bigonnet M, Blum Y, Elaroui N, Armenoult L, Ayadi M et al (2021) A transcriptomic signature to predict adjuvant gemcitabine sensitivity in pancreatic adenocarcinoma. *Ann Oncol* 32: 250–260
- O'Kane GM, Ladak F, Gallinger S (2021) Advances in the management of pancreatic ductal adenocarcinoma. *Can Med Assoc J* 193: E844–E851
- Olivares O, Mayers JR, Gouirand V, Torrence ME, Gicquel T, Borge L, Lac S, Roques J, Lavaut M-N, Berthezène P et al (2017) Collagen-derived proline promotes pancreatic ductal adenocarcinoma cell survival under nutrient limited conditions. *Nat Commun* 8: 16031
- Parker SJ, Amendola CR, Hollinshead KER, Yu Q, Yamamoto K, Encarnación-Rosado J, Rose RE, LaRue MM, Sohn ASW, Biancur DE et al (2020) Selective alanine transporter utilization creates a targetable metabolic niche in pancreatic cancer. *Cancer Discov* 10: 1018–1037
- Perez-Escuredo J, Van Hee VF, Sboarina M, Falces J, Payen VL, Pellerin L, Sonveaux P (2016) Monocarboxylate transporters in the brain and in cancer. *Biochem Biophys Acta* 1863: 2481–2497
- Rodrigues LM, Uribe-Lewis S, Madhu B, Honess DJ, Stubbs M, Griffiths JR (2017) The action of beta-hydroxybutyrate on the growth, metabolism and global histone H3 acetylation of spontaneous mouse mammary tumours: evidence of a beta-hydroxybutyrate paradox. *Cancer Metab* 5: 4
- Saraon P, Cretu D, Musrap N, Karagiannis GS, Batruch I, Drabovich AP, van der Kwast T, Mizokami A, Morrissey C, Jarvi K et al (2013) Quantitative proteomics reveals that enzymes of the ketogenic pathway are associated with prostate cancer progression. *Mol Cell Proteom* 12: 1589–1601
- Schreiber FS, Deramaudt TB, Brunner TB, Boretti MI, Gooch KJ, Stoffers DA, Bernhard EJ, Rustgi AK (2004) Successful growth and characterization of mouse pancreatic ductal cells: functional properties of the Ki-RAS(G12V) oncogene. *Gastroenterology* 127: 250–260
- Shukla SK, Gebregiworgis T, Purohit V, Chaika NV, Gunda V, Radhakrishnan P, Mehla K, Pipinos II, Powers R, Yu F et al (2014) Metabolic reprogramming induced by ketone bodies diminishes pancreatic cancer cachexia. *Cancer Metab* 2: 18
- Siegel RL, Miller KD, Jemal A (2019) Cancer statistics, 2019. *CA Cancer J Clin* 69: 7–34.
- Subramanian A, Tamayo P, Mootha VK, Mukherjee S, Ebert BL, Gillette MA, Paulovich A, Pomeroy SL, Golub TR, Lander ES et al (2005) Gene set enrichment analysis: a knowledge-based approach for interpreting genome-wide expression profiles. *Proc Natl Acad Sci USA* 102: 15545–15550
- Sui Z, Zhou J, Cheng Z, Lu P (2015) Squalene epoxidase (SQLE) promotes the growth and migration of the hepatocellular carcinoma cells. *Tumour Biol* 36: 6173–6179
- Thomas LK, Ittmann M, Cooper C (1982) The role of leucine in ketogenesis in starved rats. *Biochem J* 204: 399–403
- Tsai PY, Lee MS, Jadhav U, Naqvi I, Madha S, Adler A, Mistry M, Naumenko S, Lewis CA, Hitchcock DS et al (2021) Adaptation of pancreatic cancer cells to nutrient deprivation is reversible and requires glutamine synthetase stabilization by mTORC1. *Proc Natl Acad Sci* 118: e2003014118
- Vaziri-Gohar A, Zarei M, Brody JR, Winter JM (2018) Metabolic dependencies in pancreatic cancer. *Front Oncol* 8: 617
- Weber DD, Aminzadeh-Gohari S, Tulipan J, Catalano L, Feichtinger RG, Kofler B (2020) Ketogenic diet in the treatment of cancer – Where do we stand? *Mol Metab* 33: 102–121
- Ying H, Kimmelman A, Lyssiotis C, Hua S, Chu G, Fletcher-Sananikone E, Locasale J, Son J, Zhang H, Coloff J et al (2012) Oncogenic Kras maintains pancreatic tumors through regulation of anabolic glucose metabolism. *Cell* 149: 656–670
- Zhang S, Xie C (2017) The role of OXCT1 in the pathogenesis of cancer as a rate-limiting enzyme of ketone body metabolism. *Life Sci* 183: 110–115
- Zhang Y, Zhang T, Yang W, Chen H, Geng X, Li G, Chen H, Wang Y, Li L, Sun B (2021) Beneficial diets and pancreatic cancer: molecular mechanisms and clinical practice. *Front Oncol* 11: 630972
- Zhu XG, Chudnovskiy A, Baudrier L, Prizer B, Liu Y, Ostendorf BN, Yamaguchi N, Arab A, Tavora B, Timson R et al (2021) Functional genomics in vivo reveal metabolic dependencies of pancreatic cancer cells. *Cell Metab* 33: 211–221
- Zijlstra A, Mellor R, Panzarella G, Aimes RT, Hooper JD, Marchenko ND, Quigley JP (2002) A quantitative analysis of rate-limiting steps in the metastatic cascade using human-specific real-time polymerase chain reaction. *Cancer Res* 62: 7083–7092